Investigating the interfacial process and bulk electrode chemistry in tungsten oxide electrochromic materials

Anyang Hu

Thesis submitted to the faculty of the Virginia Polytechnic Institute and State University in partial fulfillment of the requirements for the degree of

Master of Science
In
Chemistry

Feng Lin (Chair)
Brian M. Tissue
Louis A. Madsen
Wei Zhou

September 4th, 2020
Blacksburg, VA

Keywords: electrochromism, morphological evolution, phase transformation, charge heterogeneity, durability

Investigating the interfacial process and bulk electrode chemistry in tungsten oxide electrochromic materials

Anyang Hu

Academic Abstract

The growing need for high-performance electrode materials in electrochemical conversion and storage applications requires further fundamental investigation on the working and degradation mechanisms of these materials. Among various functional materials, transition metal oxides are still one of the main choices due to their tunable chemical compositions and diverse crystal structures in most aqueous and organic electrolytes. The charge transfer process mainly occurs at the electrode–electrolyte interface, and controlling the electrochemical interfacial stability represents a key challenge in developing sustainable and cost-effective electrochromic materials. The present thesis focuses on classical tungsten trioxide (WO_3) materials as the platform to uncover the previously unknown interrelationship between phase transformation, morphological evolution, nanoscale color heterogeneity, and performance degradation in these materials during 3,000 cyclic voltammetry cycles. Through the application of novel cell design, synchrotron/electron spectroscopic, and imaging analyses, we observe that the interface between

the WO_3 electrode and 0.5 M sulfuric acid electrolyte undergoes constant changes due to the tungsten oxide dissolution and redeposition. The redeposition of dissolved tungsten species provokes *in situ* crystal growth, which ultimately leads to phase transformation from the semicrystalline WO_3 to a nanoflake-shaped, proton-trapped tungsten trioxide dihydrate ($H_xWO_3 \cdot 2H_2O$). The multidimensional (surface and bulk) quantification of the electronic structure with X-ray measurements reveals that the tungsten reduction caused by proton trapping is heterogeneous at the nanometric scale and is responsible for the nanoscale color heterogeneity. The Coulombic efficiency, optical modulation, apparent diffusion coefficients, and switching kinetics are gradually diminished during 3,000 cyclic voltammetry cycles, resulting from the structural and chemical changes of the WO_3 electrode. We hypothesize that the high interfacial reactivity in the electrode–electrolyte interfacial region could be the universal underlying mechanism leading to undesired bulk structural changes of inorganic electrochromic materials.

Investigating the interfacial process and bulk electrode chemistry in tungsten oxide electrochromic materials

Anyang Hu

General Audience Abstract

With the rapid development of human society, the research of new energy-saving materials has become a focus of attention. Among them, electrochromic devices can effectively adjust their color through a controllable electrochemical reaction and have a wide range of uses in our daily life. For example, smart windows can reduce glare and heat without blocking the natural light, thereby providing buildings and vehicles with better thermal and visual comfort. Electrochromic optical displays can lower energy consumption. Variable reflectance mirrors such as anti-glare car rear-view mirrors can ensure the safety of driving. Lastly, wearable apparel such as electrochromic lenses for spectacles and sunglasses can protect users from ultraviolet radiation. Although electrochromic materials and devices have not expanded from the niche market, the enormous potential that they hold cannot be ignored and wide-scale commercialization should be sought after.

Tungsten oxides electrochromic devices have proved to utilize the full spectrum of the incident light through structure design. These devices can also be configured with solar cells as a state-of-

art integrated self-powered system with satisfactory optical modulation that can be obtained without any external electrical energy input. Moreover, WO_3-based devices have also been combined with the electrodeposition technology to achieve fast color-switching kinetics. However, the long-term durability in the acidic electrolyte under electrochemical cycling conditions needs to be further improved, and the road of full commercialization is still unpaved.

To design high-performance electrochromic materials, it is imperative to study the degradation mechanism under long-term electrochemical cycling conditions. In the present thesis, the performance degradation of the WO_3 electrode in acid electrolytes involves chemical changes. Through a better understanding of the fundamental degradation process, the design of high-performance electrochromic metal oxides can be developed.

Acknowledgments

First, I am grateful for being instructed and guided by my advisor Dr. Feng Lin. Your pure curiosity, self-discipline, and wisdom have always inspired me on my scientific journey. I appreciate the important training I have received from you such as public presentation, scientific writing, and team working, all of which have helped me to be more prepared with future challenges. The experimental details may fade away when time goes by, but the valuable academic and personal suggestions you have shared with me will not be forgotten.

My thanks also go to all my committee members, Professors Brian Tissue, Louis Madsen, and Wei Zhou. In the past two years, as a young graduate student, I have communicated with Dr. Tissue many times to discuss how to classify countless existing literature, how to summarize useful theories, and how to improve scientific communication skills. Thanks for all your important suggestions. Dr. Madsen, I sincerely thank you for your care, the help I gained from your emails, our discussions in your office, and some causal meetings in the hallway. You are always friendly to communicate with and your profound knowledge has always broadened my horizons in chemistry. Thank you, Dr. Zhou. Your expertise in nanophotonics has enabled me to solve

problems from many other perspectives and further explore the joy of science. I sincerely thank you all for your patience and help during my graduate study.

I want to thank all my lab mates that I was fortunate enough to work with. Thanks to two post-docs, Dr. Linqin Mu and Dr. Dong Hou, for your help whenever I need it. Thank you Chunguang Kuai, Muhammad Mominur Rahman, David Kautz, Crystal Waters, Zhengrui Xu, Stephanie Spence, Tianyi Liu, Lei Tao, Zhijie Yang, Yuxin Zhang, Huabin Sun, and Mingyu Yuan for your support and friendship. Thank you, Scott McGuigan, for your wonderful work as an undergraduate student in our lab, it was a great pleasure to work with you. I wish you all the best for your graduate study at North Carolina State University.

I am also very thankful for the warmth brought by the Department of Chemistry at Virginia Tech. Specifically, Dr. John Morris, who is always listening and supportive when I need him and Ms. Joli Huynh, who always smiles at me when I ask any questions. You make me feel welcome and provide me with happy memories.

To my dearest family, my parents Hongqiao Hu and Hongling Xiong, and my fiancée Ni Yang, you are my sunshine and always stand by my side no matter what happens. You always unconditionally support me in pursuing my dreams. I love you all from the bottom of my heart.

Attributions

In this thesis, Chapter 2 is adapted from a published manuscript in the *J. Mater. Chem. A, 2020, 8, 20000-20010* (DOI: 10.1039/d0ta06612e), reproduced with permission from the Royal Society of Chemistry, where Anyang Hu is the first author. The coauthors are Zhisen Jiang, Chunguang Kuai, Scott McGuigan, Dennis Nordlund, Yijin Liu and Feng Lin. Anyang Hu performed material synthesis, characterization, and electrochemical experiments. Zhisen Jiang and Dr. Yijin Liu performed TXM at SLAC National Accelerator Laboratory. Anyang Hu. analyzed the TXM data with help from Zhisen Jiang and Dr. Yijin Liu. Chunguang Kuai performed TEM at Nanoscale Characterization and Fabrication Laboratory (NCFL, Virginia Tech). Dennis Nordlund performed soft-XAS at SLAC National Accelerator Laboratory. Scott McGuigan assisted the electrochemical measurements. Dr. Feng Lin supervised the research project, provided scientific insights during data analysis, and assisted in writing and editing.

Table of Contents

1 Introduction

Electrochromic (EC) metal oxides demonstrate distinct optical transmittance spectra, either in the visible range, ultraviolet range, or near-infrared range in response to the external electrical stimulus. The color tunability is mainly caused by the changes in the bandgap energy of the material, which is usually associated with the change of oxidation states of the material. Although various metal oxides have electrochromic properties, metal oxides which exhibit superior durability, large optical modulation (the difference between the bleached transmittance and colored transmittance), and fast switching kinetics are promising for application.[1] However, achieving superior durability has always been a challenge, and the basic mechanism of degradation is still lack of systematic research, especially for semi-crystalline WO_3 thin films. Our work focuses on understanding and controlling the degradation of ion intercalation electrochromic metal oxides, specifically tungsten trioxide (WO_3). This chapter focuses on introducing 1) The structure and working principles of electrochromic devices (ECDs). 2) Crystal structures, electronic structures, and optical properties of WO_3, as well as an important background of tungsten oxide hydrates. 3) The current understanding of the long-term durability of WO_3.

1.1. Electrochromic devices

The largest application of ECDs is “smart window” in energy-efficient buildings, which can improve the indoor comfort by dynamically controlling the light transmittance.[2] Today's EC technology is already commercial but further enhancing the material durability is of great importance. Early investigations into the durability of tungsten oxide films in acid electrolytes by Deb et al. did not provide a reliable argument to explain why degradation occurs.[3] In recent decades, how to eliminate it still a challenging research direction.[4] Considering the great achievements of the ion-intercalation chemistry in rechargeable batteries, this can provide promising insights for further study of ion-intercalation chemistry in electrochromic metal oxides, especially the mechanism of degradation. Degradation phenomena are complex and involve several factors such as the change of crystallinity, phase transformation, electronic structure evolution, transition metal oxide dissolution, morphological evolution, nanocrystal growth, mechanical failure, and other parasitic electrochemical side-reactions.[5]

1.1.1. Electrochromic device structure

Fig. 1 illustrates a general ECD design with five superimposed layer structures.[6] The central layer of an ECD is an ion conductor which conducts ions rather than electrons. Regarding the selection of intercalated ions, it is important that the ionic radius be small enough to physically pass through the cavity in the host lattice and that a thermodynamically stable intermediate can be formed during the intercalation process. Therefore, protons (H^+) and alkali metal ions (Li^+ and Na^+) are hitherto the most studied intercalating cations.[7] Transition metal oxide thin films are typical EC layers, which can conduct ions and have cathodically coloring properties (coloring with ion intercalation). Ion storage layers can also conduct ions and if possible can have anodically coloring properties (coloring with ion deintercalation), serving as a complementary electrochromic layer.[8] The above-mentioned three-layer construction is placed between two transparent electron-conductive substrates. The electron-conductive substrates can be wide-bandgap semiconductors doped with other elements, and those materials include fluorine-doped tin oxide (FTO) and indium-doped tin oxide (ITO), as well as noble metals (like Pt), carbon nanotubes (CNTs), and graphene.[9]

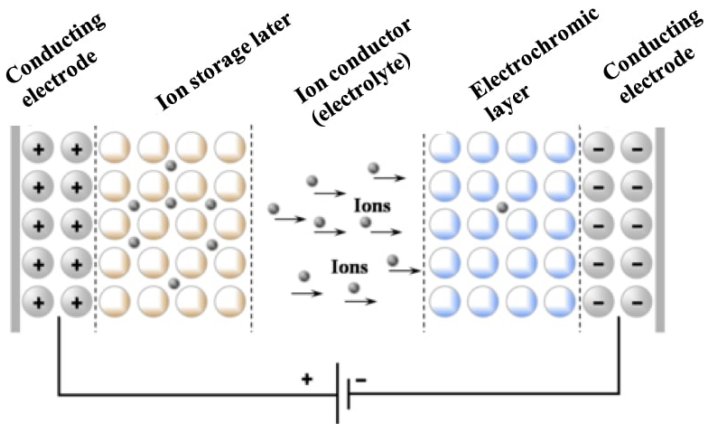

Fig. 1 General ECD configuration with five superimposed layers. Arrows illustrate the transport of cations by applying a voltage (as shown) between two transparent conductors. Adapted from reference 10 with permission. Copyright 2016, Springer Nature.

1.1.2. Electrochromic working principles

Transport of cations from the EC layer to the ion storage layer (or vice versa) is commenced by applying an electrical field between two transparent electron-conductive substrates. Concurrently, these cations are balanced by electrons transported through the external circuit. It is because of these electrons that EC layers are capable of changing color (to be discussed later). Likewise, reversing the voltage (the EC layer has a negative voltage in **Fig. 1**, otherwise it has a positive voltage) can switch the transport direction of cations and electrons and therefore the

original optical properties of the EC layer are restored. Only a small amount of charge is needed to change the color, which is beneficial to energy efficiency.[11] Moreover, ECDs are capable of maintaining their optical properties under open-circuit conditions if the system is isolated from the ambient environment and the central ion-conducting electrolyte has sufficiently low electron conductivity.

1.1.3. The influence of interface

As we introduced above, the bulk properties of each layer must match and achieve electrochromic performance. However, it is increasingly apparent that the influence of interfaces needs to be further understood in the ion intercalation/ deintercalation processes, such as the EC layer–electrolyte interface and the EC layer–substrate interface. In particular, in a lithium-ion system, certain interfacial layers between the EC layer and electrolyte can facilitate the transport of Li^+ ions across the interface, such as the formation of lithium peroxide (Li_2O_2) by conversion reactions between Li and Ni_2O_3.[12] Likewise, the interfacial layer between the EC layer and FTO substrate can improve the electron transport, such as artificially constructing of monolayer

graphene by chemical vapor deposition, which has excellent electronic conductivity and visible light transmission.[13] The ion-intercalation/deintercalation initiates at the EC layer–electrolyte interface, and advances towards the bulk lattice through solid-state diffusion.[14] Many nanostructured metal oxides have been developed due to the number of exceptional characters of nanostructures over traditional planar materials. Some of the characteristics include 1) Surface-to-volume ratio increases allowing the electrolyte infiltration and the chemical and physical interactions between EC layers and electrolyte, promoted by a larger surface area.[15] However, the appearance of the diffusion layer at the interface, the formation of interphase layers, and the evolution of interfacial speciation are highly possible to affect the long-term performance,[16] which may offset the benefits of the larger surface-to-volume ratio. 2) The surface energy changes with an increasing amount of surface species that have different bonding structures than the bulk (such as bond length, bond strength, bond angle, etc.). The varying ratio of surface energy to bulk energy can potentially assist nanocrystal growth along with specific directions.[17] 3) Nanoparticles could also have size-dependent pseudocapacitive electrochemical properties, which enable fast kinetics of surface processes rather than the slow solid-state diffusion process in the bulk.[18, 19] Nevertheless,

it is not clear which one or combination of features above can give rise to the modified electrochromic performance. Moreover, it has been reported that the heterogeneous particle-particle interactions result in degradation because electrons and cations must traverse several particle–particle interfaces during the long-term ion intercalation/ deintercalation processes.[14] Most importantly, the transition metal oxides may partially dissolve and redeposit at the EC layer–electrolyte interface. This would change the composition and nanostructure of the interface and could influence the charge transfer process, resulting in performance degradation.

1.2. Electrochromic tungsten trioxide

Tungsten trioxide (WO_3) is one of the most studied electrochromic materials and the first widely-accepted ECD based on tungsten oxide was attributed to Deb et al. in 1969.[3, 20] Thin-film WO_3 (all the W sites are W^{6+}) is initially colorless or light yellow. W^{5+} or W^{4+}sites can be generated by the electrochemical reduction and blue color that appears is seen as the electrochromic effect. It is extensively accepted that the coloration/bleaching reaction is usually as follows:

$$\mathrm{WO_3\ (colorless)} + \mathrm{x(M^+ + e^-)} \rightleftharpoons \mathrm{M}_x\mathrm{WO_3\ (blue)}$$

where M^+ stands for H^+, Li^+, or Na^+. In this thesis, we take tungsten trioxide (WO_3) as our research platform because 1) studying the electrochromic performance of WO_3, especially the degradation can further rationalize the relationship of atomic structures with macroscopic performance, and 2) the evolution of crystal phase and chemical composition of WO_3 influence the electrochromic performance including durability, optical modulation, and switching kinetics.

1.2.1. Crystal Structures

WO_3 is composed of octahedral structural units (W atoms in the middle and O in the vertices of the octahedron) arranged with the corner or edge-sharing with other octahedra.[21-23] In the ion-intercalation chemistry, the inter-octahedral spaces are important since they provide large enough space for the transport of ions. The WO_3 crystals without distortion can be viewed as a cubic structure consisting of corner-sharing WO_6 octahedron (**Fig. 2**).

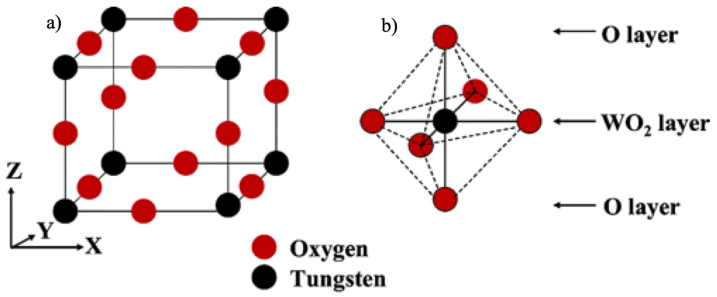

Fig. 2 The lattice structure of WO_3. a) The cubic WO_3 structure. b) The WO_6 octahedron. Reproduced from reference 24 with permission. Copyright 2006, American Chemical Society.

However, cubic WO_3 is difficult to synthesize due to its instability. Given the lattice distortion of the WO_6 octahedron (including various tilt angles and directions of rotation), several polymorphs of WO_3 have appeared. **Fig. 3** shows the lattice distortions and temperature-dependent transition among five different polymorphs. The phase transformation normally happens as follows: when the temperature is below −43 °C, it is monoclinic II (ϵ-WO_3); when the temperature increases from −43 °C to 17 °C, it becomes triclinic (δ-WO_3); when the temperature reaches between 17 °C to 330 °C, it is monoclinic I (γ-WO_3); when the temperature further raises from 330 °C to 740 °C, it becomes orthorhombic (β-WO_3); and when the temperature is above 740 °C, it owns tetragonal (α-WO_3) lattice structure.[25]

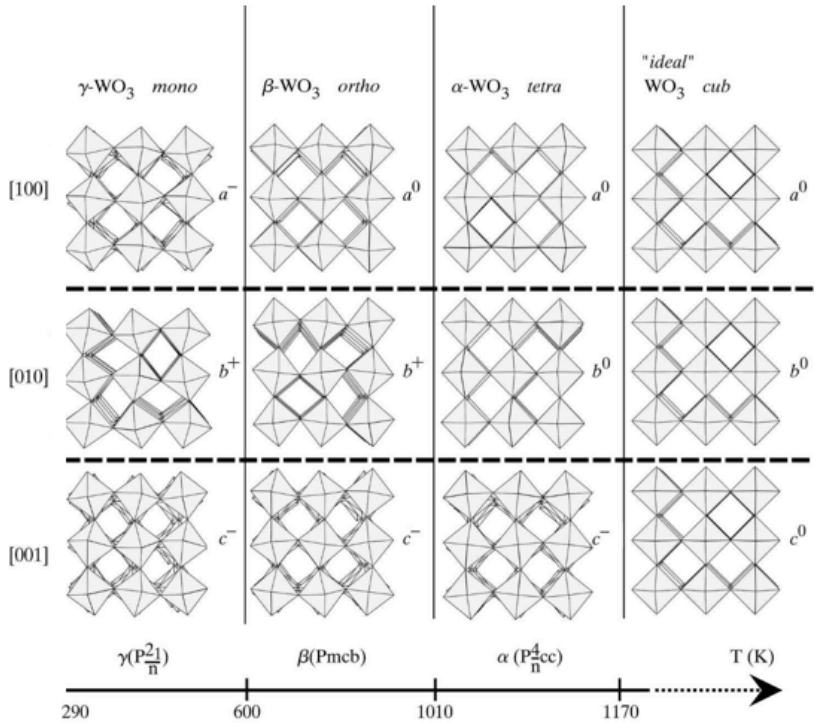

Fig. 3 The lattice patterns by tilting and the temperature-dependent transition among five different polymorphs of WO_3. A, b, and c are three Cartesian axes from the cubic orientation; the +, − and 0 represent the in-phase, out of phase and no tilting along each Cartesian axes, respectively. Adapted from reference 26 with permission. Copyright 2011, Wiley-VCH.

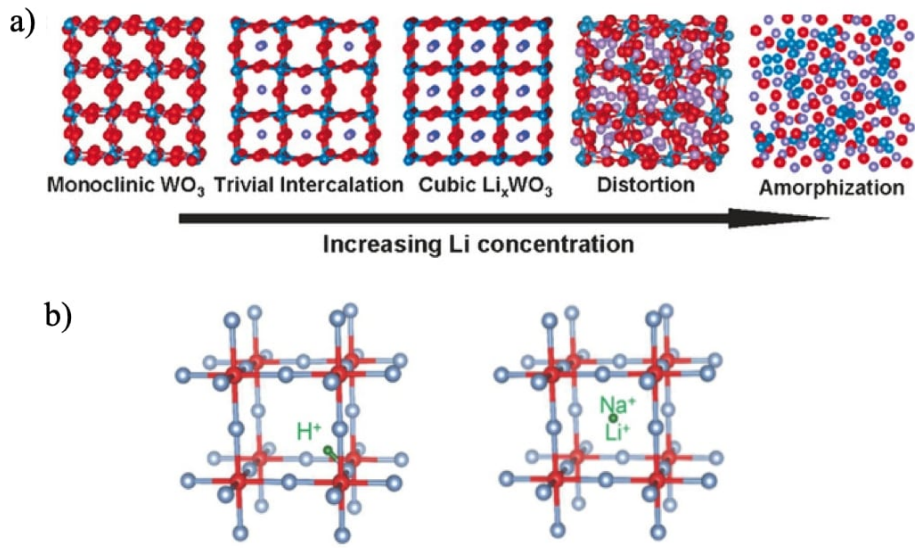

Fig. 4 a) Structure and crystal symmetry evolution in the Li_xWO_3 lattice with the increasing of Li ions concentration. Adapted from reference [27] with permission. Copyright 2016, Wiley-VCH. **b) Crystal structure of ion (Li^+, Na^+, H^+)-intercalated c-WO_3.** Adapted from reference 28 with permission. Copyright 2015, Wiley-VCH.

According to **Fig. 3**, γ-WO_3 is the most stable phase at room temperature (298.15K), but it is necessary to mention that this phase could further transform into other phases through ion intercalation. As the concentration of Li ions increases, the Li-intercalated phase gradually evolves from monoclinic crystal to cubic structure and ends in an amorphous state. (**Fig. 4a**).[27] Structurally, some studies reported that Li^+ ions and Na^+ ions are located at the centers of octahedrons without chemically bonding to the W or O sites during the intercalation process, whereas, the H^+ is likely

to form hydroxyl groups with oxygen atoms (the sites of intercalated ions in lattice structures are shown in **Fig. 4b**).[28-30]

1.2.2. Electronic structures

WO_3 is an n-type semiconductor with bandgap energy (E_g) varying from 2.6 eV to 3.25 eV.[31] Many factors can contribute to varying bandgaps of WO_3. The valence band of WO_3 is attributed to filled O(2p) orbitals while the conduction band is made up of empty W(t_{2g}) orbitals.[31] Normally, the Fermi level is located in the middle of the conduction band and the valance band, however, the Fermi level would be generally closer to the conduction band in the nonstoichiometric WO_{3-X} ($0<x<1$) or the cation intercalation M_XWO_3 (where M can be Li^+, Na^+, and H^+).[32] Interestingly, the upper moving of Fermi level is usually accompanied by a semiconductor-to-conductor transition of WO_3,[33] because of the increased free-electron density in the conduction band of WO_3. Consequently, active electrons do not need to have energy as high as that in WO_3 for jumping from the valence band into the conduction band, and therefore the electrical conductivity is enhanced.[33, 34] Besides the influence of oxygen vacancy and ion intercalation to the bandgap, another important

factor is the particle size. Experimentally, the particle size can be controlled during synthesis by adjusting the substrate temperature(T_S) in the radio frequency sputtering.[35] The typical relationship of crystal size and the bandgap is shown in **Fig. 5**, with the decrease of crystal size from 100 nm (T_s = 500 °C) to 9 nm(T_s = 100 °C). It is observed that particles with smaller size tend to have larger bandgaps. In general, the bandgap of WO_3 can be manipulated by controlling the particle sizes and crystal phases in the synthesis step. Furthermore, since the degree of phase transformation affects the occupation of the W(t_{2g}) orbital, the above-described phase transformation is often along with the change of bandgap.[36]

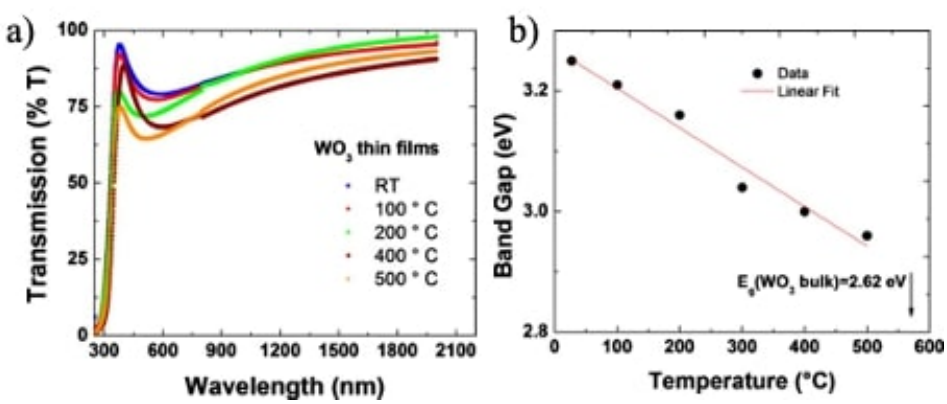

Fig. 5 a) Transmittance spectra of WO_3 thin films made by the radio frequency sputtering at different substrate temperatures (T_S). b) T_S–E_g relationship of radio frequency sputtered WO_3 films. Reproduced from reference 35 with permission. Copyright 2010, American Institute of Physics.

1.2.3. Optical properties

The optical characteristics of tungsten oxides are significant but complex in the realm of electrochromic devices.[37, 38] Until today, the most acceptable mechanism of coloration is considered as the dual injection of electrons and cations that can alter the bandgap of the host material, as proposed by Hersh et al.[39] Regarding the amorphous or low crystallinity of WO_3 thin film, Faughnan et al.[40] reported that the intervalence charge transfer (IVCT) process is responsible for the coloration mechanism. Similarly, Wittwer et al.[41] proposed that the inserted electrons are localized in W^{6+} sites to form W^{5+}, and the surrounding lattice will be polarized forming small polarons. Incident photons can be absorbed by small polarons that hop from one site to another, as seen below.

$$h\nu + W^{5+}(A) + W^{6+}(B) = W^{6+}(A) + W^{5+}(B)$$

However, Schirmer et al. proposed that inserted electrons would enter extended states of the WO_3 band structure and are scattered by impurities or defects in crystalline tungsten oxides instead of entering localized states as in amorphous tungsten oxides.[42] In general, there are two different absorption mechanisms (1) small polaron transitions for amorphous tungsten oxide films, and (2)

Drude-like free electron scattering for crystalline tungsten oxide films.[43] From another perspective, the optical transmittance spectra of WO_3 thin films in the visible region are mainly determined by the bandgap of the material.[29] The nonstoichiometric WO_{3-X} ($0<x<1$) and tungsten bronze (M_XWO_3) show a reduced bandgap (caused by the dual injection of electrons and cations), the incident photon can be partially absorbed, and the film exhibits certain blue.[44] The stoichiometric WO_3 has a full valence band and an empty conduction band, which generates a wide enough bandgap that the incident light can only transmit instead of being partially absorbed.[45] The detailed change of valence band and conducting band of tungsten oxides with different stoichiometry are shown in **Fig. 6**.[32, 46]

Based on the discussion above, crystal structures, electronic structures, and optical properties of WO_3 are closely related to each other. Their evolution during the long-term ion intercalation/ deintercalation processes is worth further research. These evolutions may play vital roles in clarifying the mechanism of degradation and provide a profound understanding of the degradation that can boost the research of developing ECDs with superior durability.

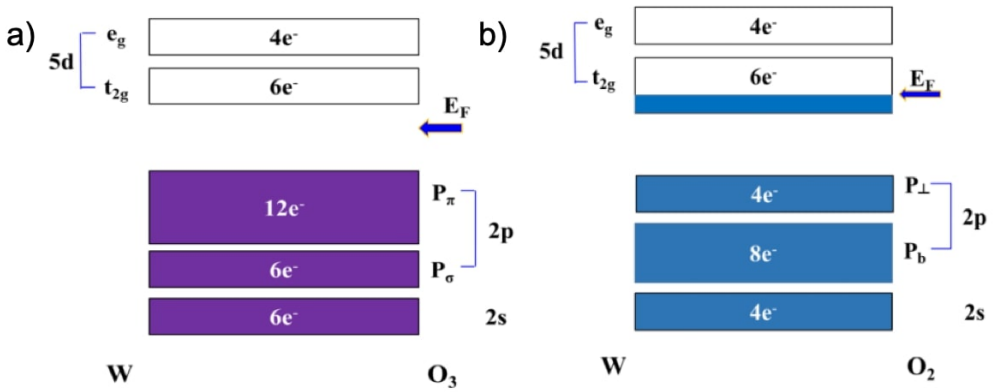

Fig. 6 Schematic band profiles of tungsten oxides. a)Tungsten trioxide; b) Tungsten dioxide. The arrow indicates the location of the Fermi level and the filled states are shaded. Reproduced from reference 32 with permission. Copyright 2006, Royal Society of Chemistry.

1.2.4. Tungsten oxide hydrates

In wet chemistry synthesis of WO_3, the formation of tungsten oxide hydrates ($WO_3 \cdot nH_2O$) is normally the first step and subsequently calcinated to obtain the desired crystal phase of WO_3. To have a clear picture of the phase transformation of WO_3, it is important to consider the crystal structure of $WO_3 \cdot nH_2O$. There are two representative kinds of hydrates: $WO_3 \cdot 2H_2O$ (dihydrate) and $WO_3 \cdot H_2O$ (monohydrate).[47] The crystal structure of tungsten oxide hydrates directly related to the water content and water molecule position in the WO_3 lattice.

$WO_3 \cdot 2H_2O$ has a layered structure, consisting of layers of $WO_5(OH_2)$ octahedra by corner-sharing. One of the oxygen atoms is replaced by one water molecule at the vertex position. The other confined water layer is connected by hydrogen bonds inside the crystal lattice. The interlayer spacing is assigned around 6.96 Å by Liang et al.[48] Dehydrating at 120 °C yields $WO_3 \cdot H_2O$, which is composed of distorted corner shared $WO_5(OH_2)$ octahedra, coordinated by five oxygen atoms and one water molecule and there is no confined water layer between the layers and interlayer distance is decreased to 5.33 Å given by Kattouf et al.[49] The crystal structures of these two tungsten oxide hydrates with interlayer spacing are shown in Figure 7. Calcining at temperatures above 350 °C yields the anhydrous WO_3, which exhibits a monoclinic crystal structure of the corner-sharing octahedra. The typical crystal structure evolution with the loss of confined water is proposed by Augustyn et al.[50], as shown in **Fig. 7**. Regardless of tungsten oxide or tungsten oxide hydrates, considering the size of the cavity and the interlayer spacing, it is possible to have ions intercalation into the lattice such as H^+, Li^+, Na^+, even with certain solvent molecules like water as hydroniums.[51] Therefore, the effect of solvent molecules should be considered during under long-term ion intercalation/deintercalation, especially in aqueous electrolytes.

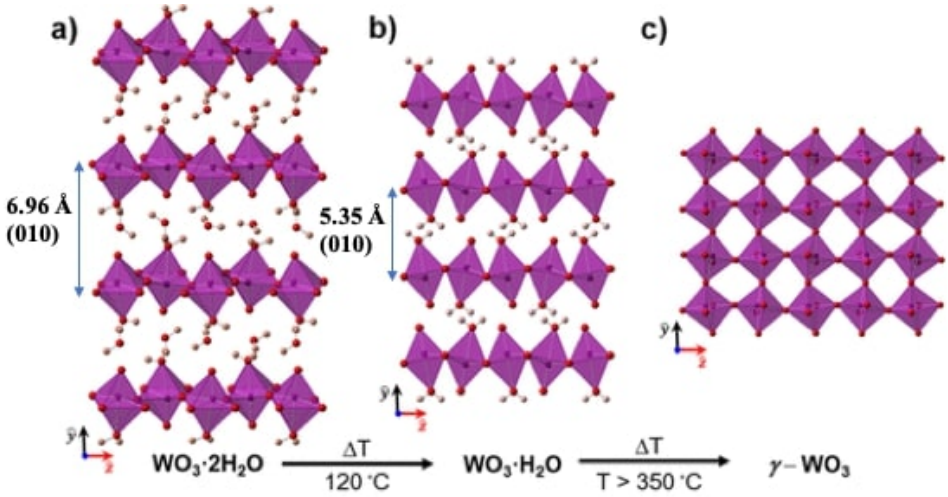

Fig. 7 Crystal structures and phase transformation of tungsten oxide hydrates. a). $WO_3 \cdot 2H_2O$ (monoclinic).b). $WO_3 \cdot H_2O$ (orthorhombic); c) WO_3 (monoclinic). Adapted from references 49, 50 with permission. Copyright 2009, Royal Society of Chemistry; Copyright 2019, American Chemical Society.

1.3. Methods for improving long-term durability

Long-term durability is the main prerequisite for practical applications of ECDs and this topic has been studied extensively.[52-60] For the sake of clarity, durability here signifies the ability to maintain the reversible charge transport over thousands of cycles without large efficiency loss, including stable optical modulation, little or no attenuation with peak current density or charge/discharge capacity, and constant switching kinetics without sluggishness. Several methods of rejuvenation of WO_3 have been developed under galvanostatic (constant current)[53] and

potentiostatic (constant potential) treatments in organic electrolyte.[61, 62] The experience of using organic electrolytes (Li-ion intercalation) can help the investigation of using aqueous electrolytes (proton intercalation). Here, three approaches 1) post-electrochemical treatment, 2) pre-electrochemical treatment, and 3) designing oxide mixtures can be used to mitigate the degradation and rejuvenate WO_3 thin films in the organic electrolyte.

1.3.1. Post-electrochemical treatment

Most studies of post-electrochemical treatment have been carried out on tungsten oxides including galvanostatic[61] and potentiostatic[62] two post-treatments. These methods open the door to study the degradation of ECDs. **Fig. 8** shows the first systematic study of degraded WO_3 thin films in the organic electrolyte by Wen et al.[61] Specifically, cyclic voltammetry (CV) measurements are utilized to detect the attenuation of peak current density in **Fig. 8a** and in-situ transmittance measurements directly monitor the real-time shrinkage of optical modulation in **Fig. 8c**. The performance degradation can be attributed to Li ion-trapping inside the host lattice based on two assumptions: (1) tungsten oxide is composed of a network of sites with various energy

barriers; (2) for those low-energy barrier sites, ions can diffuse rapidly throughout the lattice structure, but for other sites with higher-energy barriers, reversible ion intercalation/ deintercalation is not allowed because ion-trapping at those sites is thermodynamically preferred.[63-67] To de-trap the ions, a constant current can be applied and held for 20 h, the eventual potential is built up to 5.5 V vs Li/Li^+ in **Fig. 8b.** The optical transmittance is recovered after this post-electrochemical treatment as shown in **Fig. 8c** and **8d**. The rejuvenated film can display a similar CV curve to the pristine film as indicated in **Fig. 8a.** All of the above phenomena point out that it is possible to eliminate the trapping of ions in WO_3 thin films after long-term electrochemical cycling by applying a constant current as the post-electrochemical treatment. The similar galvanostatic rejuvenation has been successfully proved in TiO_2 and MoO_3 EC films as well.[68, 69] It seems to be effective at increasing the life-time of ECDs by simply applying a constant current. However, the high potential will generate unpredicted side reactions at the EC layer–electrolyte interface, the uncertain effect of high potential in this method requires further investigation.

Besides the galvanostatic rejuvenation described in **Fig. 8,** it is intuitive to utilize constant potential (potentiostatic) as post-treatment to rejuvenate the degraded WO_3 thin films, **Fig. 9** describes one of the representative results by Arvizu et al. [62] The optical transmittance decreases dramatically in **Fig. 9a,** indicating degradation. And similarly, this optical performance can be recovered when a 5.55 V vs Li/Li^+ constant potential is applied and held for about 20 hours. The rejuvenation phenomenon can be also be seen in the plot of optical transmittance vs. time over the entire visible light range in **Fig. 9b**. The films after de-trapping have almost the same optical modulation as the pristine films. This helps prove that the post-electrochemical treatment effectively demonstrates the de-trapping of Li^+. There is also more evidence that the trapped Li-ions can be de-trapped using time-of-flight elastic recoil detection analysis (ToF-ERDA)[70] and time-of-flight secondary ion mass spectroscopy (ToF-SIMS) according to Baloukas et al.[71] However, both galvanostatic and potentiostatic treatment needs the voltage to exceed ~5 V vs. Li/Li^+, which is way above the decomposition potential (~4.7 V vs. Li/Li^+) of the organic electrolyte ($LiClO_4$–PC).[72] That high potential would inevitably generate the decomposition of electrolyte at the EC layer–electrolyte interface, which could consume the intercalated Li^+ through

the formation of Li_2O or Li_2CO_3. Besides, the fluorine atom from the FTO substrate or indium atom from the ITO substrate may be intermixed with or diffuse into the WO_3 layer at high potential. The stability of the electron-conducting substrate, EC layer, is unclear. The real mechanisms of post-electrochemical treatments with a constant current or constant potential are not solely dependent on de-trapping ions from the host lattice. The effect of electrolyte decomposition, the preferable trapped sites in host lattice, and the modification at the EC layer–electrolyte interface and EC layer–substrate interface require more investigation.

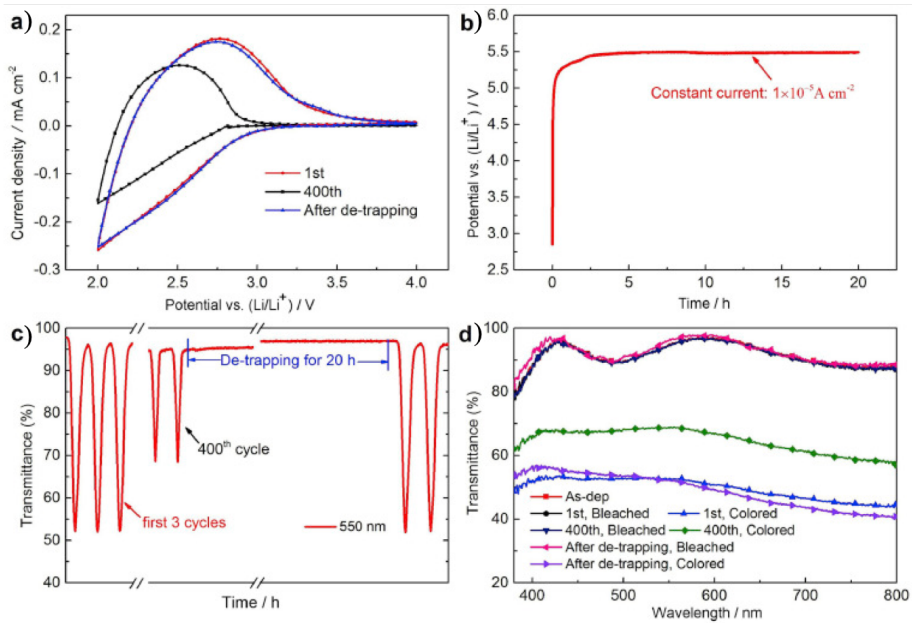

Fig. 8 Galvanostatic post electrochemical treatment of an EC WO_3 film, showing electrochemical cycling and optical transmittance performance in an organic Li-ion electrolyte. a) CV plots of WO_3 films before and after

treatment; b) Potential vs. time plot of applied constant current; c) the optical transmittance vs. time at 550 nm wavelength; d) the optical transmittance vs. time at the entire visible light range. Reproduced from reference 73 with permission. Copyright 2015, Springer Nature.

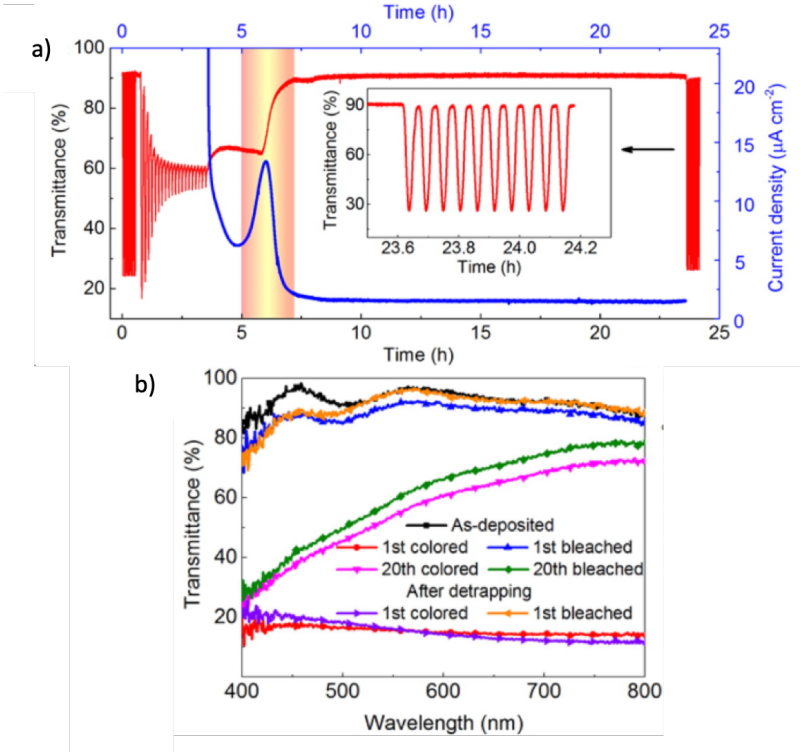

Fig. 9 Electrochemical and optical performance of amorphous WO3 films. a) In situ optical transmittance vs. time at a wavelength of 550 nm under potentiostatic de-trapping. b) In situ optical transmittance at a wavelength range of 400 nm to 800 nm. Reproduced from reference 62 with permission. Copyright 2016, American Chemical Society.

1.3.2. Pre-electrochemical treatment

Inspired by the post-electrochemical treatment, pre-electrochemical treatment has been developed to mitigate or eliminate degradation. **Fig. 10** describes one of the representative studies by Qu et al. [56] It is shown that the cycling durability of WO_3 films can be improved by immersion in the electrolyte with a constant potential of 6 V vs. Li/Li^+ for several hours before electrochemical cycling. The pre-electrochemical treatment can guarantee the efficient Li^+ de-intercalation due to the polarity of the voltage and occupation sites as well as energy barriers in the WO_3 lattice being rearranged.[56] The CV plots of no pre-electrochemical treatment WO_3 film shrink rapidly within 40 cycles. However, the WO_3 films with pre-electrochemical treatment exhibit less decline in peak current density in CV (**Fig. 10a** and **10b).**

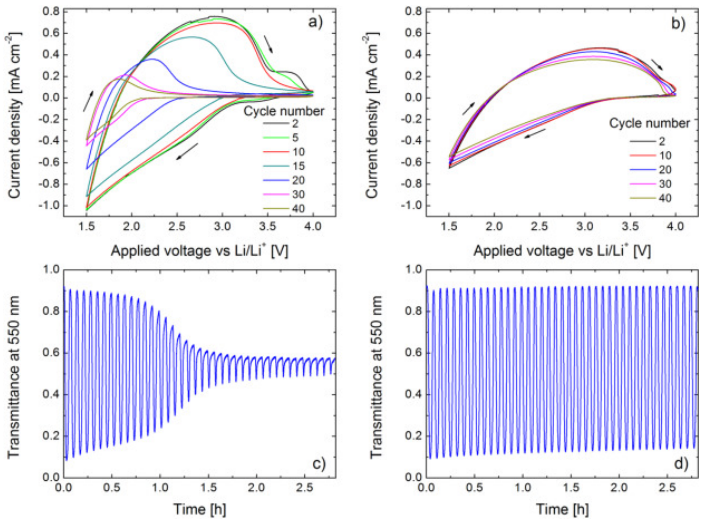

Fig. 10 The effect of pre-electrochemical treatment on WO_3 thin films. a) and b) exhibit the electrochemical cycling performance of WO_3 film without and with pre-electrochemical. c) and d) are optical transmittance vs. time at the wavelength of 550 nm without and with pre-electrochemical. Reproduced from reference 56 with permission. Copyright 2018, Elsevier.

1.3.3. Mixed-oxides

Apart from the above-mentioned post/pre-electrochemical treatments, there is another approach to improve cycling durability, designing mixed oxides. Specifically, the electrochromic performance can be improved by the combination of absorption bands of individual oxides, the synergetic electrochemical interaction between individual oxides, and the complementary match with each crystal structure. Among various studies, binary oxide mixtures are the most common choices due to the relatively low possibility of crystal mismatches, such as W oxide mixed with Ti, V, Nb, Mo, Ta, or Ti. [54, 74, 75] One example in **Fig. 11** is the W-Ti binary oxide mixture reported by Triana et al.[54] Clearly, there is an obvious decline of peak current density over time of undoped WO_3 film but relatively less attenuation in the CV plots of $W_{0.88}Ti_{0.12}O_3$ film (**Fig. 11a** and **11b**),

which demonstrates the beneficial effect of doping Ti on mitigating the degradation. Beyond binary metal oxide mixtures, it is also possible to optimize the electrochromic performance by designing ternary oxide mixtures.[76] Ti and Mo dual-doping into WO_3 like $W_{1-x-y}Ti_xMo_yO_3$ with $x < 0.2$ and $y < 0.2$ is illustrated by Niklasson et al.[55] The function of Ti is discussed above and the doping of Mo is considered because it can exhibit complementary color relative to W.[77] Similar work uses Ti and Ni dual-doping into the WO_3 films like $W_{1-x-y}Ni_xTi_yO_3$ with $x < 0.4$ and $y < 0.2$ by Morales et al.[78] However, the general rules of doping cations into host metal oxides require an in-depth investigation. The underlying principles like the selection rule of dopants, the distribution of dopants in the lattice, and the surface reconstruction of surface are still unclear. Therefore, cation doping into the transition metal oxide with the aim of superior long-term durability is one of my research focuses.

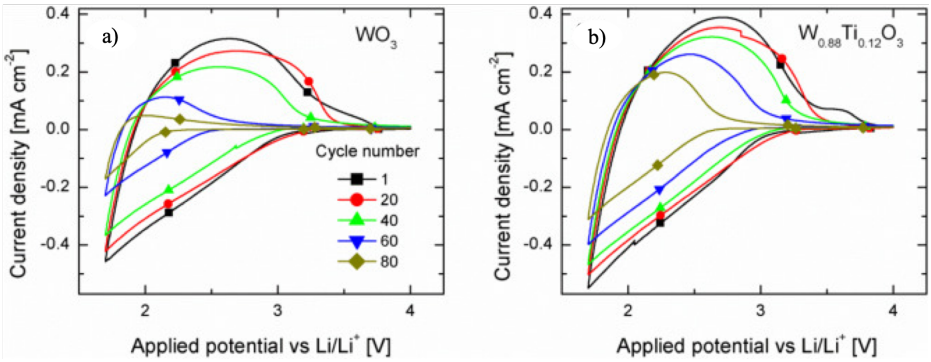

Fig. 11 Cyclic voltammetry of undoped (a) and Ti-doped (b) WO_3 thin films within the same number of CV cycles.

Reproduced from reference 54 with permission. Copyright 2014, Elsevier.

The aforementioned evidence in the literature indicates that the long-term durability study of WO_3 thin films in organic electrolyte maintains many unsolved challenges. The proposed post- and pre- electrochemical treatments lack scientific explanations of the role of the electrolyte decomposition, the phase transformation, the ion-trapping sites in the host lattice, and the interfacial morphological evolution. Hence, my research will be dedicated to studying the degradation mechanism of WO_3 thin films, and also clarifying the interrelationship between the evolution of chemical composition, phase transformation, and the degradation of WO_3 thin films during the long-term electrochemical intercalation/ deintercalation processes.

1.4. References

1. Monk, P.; Mortimer, R.; Rosseinsky, D., *Electrochromism and electrochromic devices*. Cambridge University Press: 2007.

2. Granqvist, C. G. J. T. s. f., Electrochromics for smart windows: Oxide-based thin films and devices. **2014,** *564*, 1-38.

3. Deb, S. K., Optical and Photoelectric Properties and Color Centers in Thin-Films of Tungsten Oxide. *Philos Mag* **1973,** *27* (4), 801-822.

4. Granqvist, C. G.; Arvizu, M. A.; Pehlivan, I. B.; Qu, H. Y.; Wen, R. T.; Niklasson, G. A., Electrochromic materials and devices for energy efficiency and human comfort in buildings: A critical review. *Electrochim Acta* **2018,** *259*, 1170-1182.

5. Du, M. J.; Liao, K. M.; Lu, Q.; Shao, Z. P., Recent advances in the interface engineering of solid-state Li-ion batteries with artificial buffer layers: challenges, materials, construction, and characterization. *Energ Environ Sci* **2019,** *12* (6), 1780-1804.

6. Granqvist, C.-G. J. E. M.; Devices. Wiley-VCH Weinheim, G., Electrochromic metal oxides: an introduction to materials and devices. **2015**.

7. Wu, W.; Wang, M.; Ma, J. M.; Cao, Y. L.; Deng, Y. H., Electrochromic Metal Oxides: Recent Progress and Prospect. *Adv Electron Mater* **2018,** *4* (8).

8. Granqvist, C. R., Electrochromic materials: Out of a niche. *Nat Mater* **2006,** *5* (2), 89-90.

9. Ginley, D. S.; Hosono, H.; Paine, D. C., Handbook of transparent conductors. **2010**.

10. Patel, K. J.; Bhatt, G. G.; Ray, J. R.; Suryavanshi, P.; Panchal, C. J., All-inorganic solid-state electrochromic devices: a review. *J Solid State Electr* **2017,** *21* (2), 337-347.

11. DeForest, N.; Shehabi, A.; Selkowitz, S.; Milliron, D. J., A comparative energy analysis of three electrochromic glazing technologies in commercial and residential buildings. *Appl Energ* **2017,** *192*, 95-109.

12. Lin, F.; Nordlund, D.; Weng, T. C.; Sokaras, D.; Jones, K. M.; Reed, R. B.; Gillaspie, D. T.; Weir, D. G. J.; Moore, R. G.; Dillon, A. C.; Richards, R. M.; Engtrakul, C., Origin of Electrochromism in High-Performing Nanocomposite Nickel Oxide. *Acs Appl Mater Inter* **2013,** *5* (9), 3643-3649.

13. Lin, F.; Bult, J. B.; Nanayakkara, S.; Dillon, A. C.; Richards, R. M.; Blackburn, J. L.; Engtrakul, C., Graphene as an Efficient Interfacial Layer for Electrochromic Devices. *Acs Appl Mater Inter* **2015,** *7* (21), 11330-11336.

14. Evans, R. C.; Ellingworth, A.; Cashen, C. J.; Weinberger, C. R.; Sambur, J. B., Influence of single-nanoparticle electrochromic dynamics on the durability and speed of smart windows. *P Natl Acad Sci USA* **2019,** *116* (26), 12666-12671.

15. Okubo, M.; Hosono, E.; Kim, J.; Enomoto, M.; Kojima, N.; Kudo, T.; Zhou, H. S.; Honma, I., Nanosize effect on high-rate Li-ion intercalation in LiCoO2 electrode. *J Am Chem Soc* **2007,** *129* (23), 7444-7452.

16. Augustyn, V.; McDowell, M. T.; Vojvodic, A., Toward an Atomistic Understanding of Solid-State Electrochemical Interfaces for Energy Storage. *Joule* **2018,** *2* (11), 2189-2193.

17. Llordes, A.; Garcia, G.; Gazquez, J.; Milliron, D. J., Tunable near-infrared and visible-light transmittance in nanocrystal-in-glass composites. *Nature* **2013,** *500* (7462), 323-326.

18. Augustyn, V.; Simon, P.; Dunn, B., Pseudocapacitive oxide materials for high-rate electrochemical energy storage. *Energ Environ Sci* **2014,** *7* (5), 1597-1614.

19. Yang, P. H.; Sun, P.; Du, L. H.; Liang, Z. M.; Xie, W. G.; Cai, X.; Huang, L. H.; Tan, S. Z.; Mai, W. J., Quantitative Analysis of Charge Storage Process of Tungsten Oxide that Combines Pseudocapacitive and Electrochromic Properties. *J Phys Chem C* **2015,** *119* (29), 16483-16489.

20. Deb, S. K., A novel electrophotographic system. *Applied optics* **1969,** *8 Suppl 1*, 192-5.

21. Burkhardt, S.; Elm, M. T.; Lani-Wayda, B.; Klar, P. J., In Situ Monitoring of Lateral Hydrogen Diffusion in Amorphous and Polycrystalline WO3 Thin Films. *Adv Mater Interfaces* **2018,** *5* (6).

22. Cai, G. F.; Tu, J. P.; Zhou, D.; Li, L.; Zhang, J. H.; Wang, X. L.; Gu, C. D., The direct growth of a WO3 nanosheet array on a transparent conducting substrate for highly efficient electrochromic and electrocatalytic applications. *Crystengcomm* **2014,** *16* (30), 6866-6872.

23. Cai, G. F.; Eh, A. L. S.; Ji, L.; Lee, P. S., Recent Advances in Electrochromic Smart Fenestration. *Adv Sustain Syst* **2017,** *1* (12).

24. Ramana, C. V.; Utsunomiya, S.; Ewing, R. C.; Julien, C. M.; Becker, U., Structural stability and phase transitions in WO3 thin films. *J Phys Chem B* **2006,** *110* (21), 10430-10435.

25. Vogt, T.; Woodward, P. M.; Hunter, B. A., The high-temperature phases of WO3. *J Solid State Chem* **1999,** *144* (1), 209-215.

26. Zheng, H. D.; Ou, J. Z.; Strano, M. S.; Kaner, R. B.; Mitchell, A.; Kalantar-Zadeh, K., Nanostructured Tungsten Oxide - Properties, Synthesis, and Applications. *Adv Funct Mater* **2011,** *21* (12), 2175-2196.

27. He, Y.; Gu, M.; Xiao, H. Y.; Luo, L. L.; Shao, Y. Y.; Gao, F.; Du, Y. G.; Mao, S. X.; Wang, C. M., Atomistic Conversion Reaction Mechanism of WO3 in Secondary Ion Batteries of Li, Na, and Ca. *Angew Chem Int Edit* **2016,** *55* (21), 6244-6247.

28. Huang, Z. F.; Song, J. J.; Pan, L.; Zhang, X. W.; Wang, L.; Zou, J. J., Tungsten Oxides for Photocatalysis, Electrochemistry, and Phototherapy. *Advanced Materials* **2015,** *27* (36), 5309-5327.

29. Hjelm, A.; Granqvist, C. G.; Wills, J. M., Electronic structure and optical properties of WO3, LiWO3, NaWO3, and HWO3. *Phys Rev B* **1996,** *54* (4), 2436-2445.

30. Wiseman, P.; Dickens, P., The crystal structure of cubic hydrogen tungsten bronze. *J Solid State Chem* **1973,** *6* (3), 374-377.

31. Wang, F. G.; Di Valentin, C.; Pacchioni, G., Electronic and Structural Properties of WO3: A Systematic Hybrid DFT Study. *J Phys Chem C* **2011,** *115* (16), 8345-8353.

32. Niklasson, G. A.; Granqvist, C. G., Electrochromics for smart windows: thin films of tungsten oxide and nickel oxide, and devices based on these. *J Mater Chem* **2007,** *17* (2), 127-156.

33. Mitchell, J. B.; Lo, W. C.; Genc, A.; LeBeau, J.; Augustyn, V., Transition from Battery to Pseudocapacitor Behavior via Structural Water in Tungsten Oxide. *Chem Mater* **2017,** *29* (9), 3928-3937.

34. Agrawal, A.; Cho, S. H.; Zandi, O.; Ghosh, S.; Johns, R. W.; Milliron, D. J., Localized Surface Plasmon Resonance in Semiconductor Nanocrystals. *Chem Rev* **2018,** *118* (6), 3121-3207.

35. Gullapalli, S. K.; Vemuri, R. S.; Ramana, C. V., Structural transformation induced changes in the optical properties of nanocrystalline tungsten oxide thin films. *Appl Phys Lett* **2010,** *96* (17).

36. Gillet, M.; Aguir, K.; Lemire, C.; Gillet, E.; Schierbaum, K., The structure and electrical conductivity of vacuum-annealed WO3 thin films. *Thin Solid Films* **2004,** *467* (1-2), 239-246.

37. Bondarenko, N.; Eriksson, O.; Skorodumova, N. V., Polaron mobility in oxygen-deficient and lithium-doped tungsten trioxide. *Phys Rev B* **2015,** *92* (16).

38. Hamdi, H.; Salje, E. K. H.; Ghosez, P.; Bousquet, E., First-principles reinvestigation of bulk WO3. *Phys Rev B* **2016,** *94* (24).

39. Hersh, H. N.; Kramer, W. E.; Mcgee, J. H., Mechanism of Electrochromism in Wo3. *Appl Phys Lett* **1975,** *27* (12), 646-648.

40. Faughnan, B. W.; Crandall, R. S.; Heyman, P. M., Electrochromism in Wo3 Amorphous Films. *Rca Rev* **1975,** *36* (1), 177-197.

41. Wittwer, V.; Schirmer, O. F.; Schlotter, P., Disorder Dependence and Optical Detection of Anderson Transition in Amorphous Hxwo3 Bronzes. *Solid State Commun* **1978,** *25* (12), 977-980.

42. Schirmer, O. F.; Wittwer, V.; Baur, G.; Brandt, G., Dependence of Wo-3 Electrochromic Absorption on Crystallinity. *J Electrochem Soc* **1977,** *124* (5), 749-753.

43. Santos, L.; Wojcik, P.; Pinto, J. V.; Elangovan, E.; Viegas, J.; Pereira, L.; Martins, R.; Fortunato, E., Structure and Morphologic Influence of WO3 Nanoparticles on the Electrochromic Performance of Dual-Phase a-WO3/WO3 Inkjet Printed Films. *Adv Electron Mater* **2015,** *1* (1-2).

44. Chang, M. T.; Chou, L. J.; Chueh, Y. L.; Lee, Y. C.; Hsieh, C. H.; Chen, C. D.; Lan, Y. W.; Chen, L. J., Nitrogen-doped tungsten oxide nanowires: Low-temperature synthesis on Si, and electrical, optical, and field-emission properties. *Small* **2007,** *3* (4), 658-664.

45. Cong, S.; Geng, F. X.; Zhao, Z. G., Tungsten Oxide Materials for Optoelectronic Applications. *Adv Mater* **2016,** *28* (47), 10518-10528.

46. Newman, D. J.; Ng, B., *Crystal field handbook*. Cambridge University Press: 2007.

47. Kuti, L. M.; Bhella, S. S.; Thangadurai, V., Revisiting Tungsten Trioxide Hydrates (TTHs) Synthesis - Is There Anything New? *Inorg Chem* **2009,** *48* (14), 6804-6811.

48. Liang, L.; Zhang, J. J.; Zhou, Y. Y.; Xie, J. F.; Zhang, X. D.; Guan, M. L.; Pan, B. C.; Xie, Y., High-performance flexible electrochromic device based on facile semiconductor-to-metal transition realized by WO3 center dot 2H(2)O ultrathin nanosheets. *Sci Rep-Uk* **2013,** *3*.

49. Kattouf, B.; Frey, G. L.; Siegmann, A.; Ein-Eli, Y., Enhanced reversible electrochromism via in situ phase transformation in tungstate monohydrate. *Chem Commun* **2009,** (47), 7396-7398.

50. Mitchell, J. B.; Geise, N. R.; Paterson, A. R.; Osti, N. C.; Sun, Y. Y. L.; Fleischmann, S.; Zhang, R.; Madsen, L. A.; Toney, M. F.; Jiang, D. E.; Kolesnikov, A. I.; Mamontov, E.; Augustyn, V., Confined Interlayer Water Promotes Structural Stability for High-Rate

Electrochemical Proton Intercalation in Tungsten Oxide Hydrates. *Acs Energy Lett* **2019,** *4* (12), 2805-2812.

51. Jiang, H.; Hong, J. J.; Wu, X. Y.; Surta, T. W.; Qi, Y. T.; Dong, S. Y.; Li, Z. F.; Leonard, D. P.; Holoubek, J. J.; Wong, J. C.; Razink, J. J.; Zhang, X. G.; Ji, X. L., Insights on the Proton Insertion Mechanism in the Electrode of Hexagonal Tungsten Oxide Hydrate. *Journal of the American Chemical Society* **2018,** *140* (37), 11556-11559.

52. Czanderna, A. W.; Benson, D. K.; Jorgensen, G. J.; Zhang, J. G.; Tracy, C. E.; Deb, S. K., Durability issues and service lifetime prediction of electrochromic windows for buildings applications. *Sol Energ Mat Sol C* **1999,** *56* (3-4), 419-436.

53. Lampert, C. M.; Agrawal, A.; Baertlien, C.; Nagai, J., Durability evaluation of electrochromic devices - an industry perspective. *Sol Energ Mat Sol C* **1999,** *56* (3-4), 449-463.

54. Arvizu, M. A.; Triana, C. A.; Stefanova, B. I.; Granqvist, C. G.; Niklasson, G. A., Electrochromism in sputter-deposited W-Ti oxide films: Durability enhancement due to Ti. *Sol Energ Mat Sol C* **2014,** *125*, 184-189.

55. Arvizu, M. A.; Niklasson, G. A.; Granqvist, C. G., Electrochromic W(1-x-y)Ti(x)lo(y)O(3) Thin Films Made by Sputter Deposition: Large Optical Modulation, Good Cycling Durability, and Approximate Color Neutrality. *Chem Mater* **2017,** *29* (5), 2246-2253.

56. Arvizu, M. A.; Qu, H. Y.; Niklasson, G. A.; Granqvist, C. G., Electrochemical pretreatment of electrochromic WO3 films gives greatly improved cycling durability. *Thin Solid Films* **2018,** *653*, 1-3.

57. Arvizu, M. A.; Qu, H. Y.; Cindemir, U.; Qiu, Z.; Rojas-Gonzalez, E. A.; Primetzhofer, D.; Granqvist, C. G.; Osterlund, L.; Niklasson, G. A., Electrochromic WO3 thin films attain unprecedented durability by potentiostatic pretreatment. *J Mater Chem A* **2019,** *7* (6), 2908-2918.

58. Niklasson, G. A.; Wen, R. T.; Qu, H. Y.; Arvizu, M. A.; Granqvist, C. G., Durability of Electrochromic Films: Aging Kinetics and Rejuvenation. *Ecs Transactions* **2017,** *77* (11), 1659-1669.

59. Qu, H. Y.; Rojas-Gonzalez, E. A.; Granqvist, C. G.; Niklasson, G. A., Potentiostatically pretreated electrochromic tungsten oxide films with enhanced durability: Electrochemical processes at interfaces of indium-tin oxide. *Thin Solid Films* **2019,** *682*, 163-168.

60. Wen, R. T.; Granqvist, C. G.; Niklasson, G. A., Cyclic voltammetry on sputter-deposited films of electrochromic Ni oxide: Power-law decay of the charge density exchange. *Appl Phys Lett* **2014,** *105* (16).

61. Wen, R. T.; Granqvist, C. G.; Niklasson, G. A., Eliminating degradation and uncovering ion-trapping dynamics in electrochromic WO3 thin films. *Nature Materials* **2015,** *14* (10), 996-+.

62. Wen, R. T.; Arvizu, M. A.; Morales-Luna, M.; Granqvist, C. G.; Niklasson, G. A., Ion Trapping and Detrapping in Amorphous Tungsten Oxide Thin Films Observed by Real-Time Electro-Optical Monitoring. *Chem Mater* **2016,** *28* (13), 4670-4676.

63. Bisquert, J., Analysis of the kinetics of ion intercalation - Ion trapping approach to solid-state relaxation processes. *Electrochimica Acta* **2002,** *47* (15), 2435-2449.

64. Bisquert, J.; Vikhrenko, V. S., Analysis of the kinetics of ion intercalation. Two state model describing the coupling of solid state ion diffusion and ion binding processes. *Electrochim Acta* **2002,** *47* (24), 3977-3988.

65. Bisquert, J., Beyond the quasistatic approximation: Impedance and capacitance of an exponential distribution of traps. *Phys Rev B* **2008,** *77* (23).

66. Fabregat-Santiago, F.; Garcia-Belmonte, G.; Bisquert, J.; Ferriols, N. S.; Bueno, P. R.; Longo, E.; Antón, J. S.; Castro-García, S. J. J. o. T. E. S., Dynamic processes in the coloration of WO 3 by lithium insertion. **2001,** *148* (7), E302-E309.

67. Garcia-Belmonte, G.; Bueno, P. R.; Fabregat-Santiago, F.; Bisquert, J., Relaxation processes in the coloration of amorphous WO3 thin films studied by combined impedance and electro-optical measurements. *J Appl Phys* **2004,** *96* (1), 853-859.

68. Wen, R. T.; Niklasson, G. A.; Granqvist, C. G., Eliminating Electrochromic Degradation in Amorphous TiO2 through Li-Ion Detrapping. *Acs Appl Mater Inter* **2016,** *8* (9), 5777-5782.

69. Arvizu, M. A.; Granqvist, C. G.; Niklasson, G. A., Rejuvenation of degraded electrochromic MoO3 thin films made by DC magnetron sputtering: Preliminary results. *Inera Conference: Vapor Phase Technologies for Metal Oxide and Carbon Nanostructures* **2016,** *764*.

70. Arvizu, M. A.; Wen, R. T.; Primetzhofer, D.; Klemberg-Sapieha, J. E.; Martinu, L.; Niklasson, G. A.; Granqvist, C. G., Galvanostatic Ion Detrapping Rejuvenates Oxide Thin Films. *Acs Appl Mater Inter* **2015,** *7* (48), 26387-26390.

71. Baloukas, B.; Arvizu, M. A.; Wen, R. T.; Niklasson, G. A.; Granqvist, C. G.; Vernhes, R.; Klemberg-Sapieha, J. E.; Martinu, L., Galvanostatic Rejuvenation of Electrochromic WO3 Thin Films: Ion Trapping and Detrapping Observed by Optical Measurements and by Time-of-Flight Secondary Ion Mass Spectrometry. *Acs Appl Mater Inter* **2017,** *9* (20), 16996-17002.

72. An, S. J.; Li, J. L.; Daniel, C.; Mohanty, D.; Nagpure, S.; Wood, D. L., The state of understanding of the lithium-ion-battery graphite solid electrolyte interphase (SEI) and its relationship to formation cycling. *Carbon* **2016,** *105*, 52-76.

73. Wen, R. T.; Granqvist, C. G.; Niklasson, G. A., Eliminating degradation and uncovering ion-trapping dynamics in electrochromic WO3 thin films. *Nat Mater* **2015,** *14* (10), 996-1001.

74. Martin, J.; Jack, M.; Hakimian, A.; Vaillancourt, N.; Villemure, G., Electrodeposition of Ni-Al layered double hydroxide thin films having an inversed opal structure: Application as electrochromic coatings. *J Electroanal Chem* **2016,** *780*, 217-224.

75. Wen, R. T.; Niklasson, G. A.; Granqvist, C. G., Electrochromic Iridium-Containing Nickel Oxide Films with Excellent Electrochemical Cycling Performance. *J Electrochem Soc* **2016,** *163* (2), E7-E13.

76. Sato, S.; Seino, Y. J. E.; Japan, C. i., Electrochromism in evaporated WO3-MoO3-V2O5 films. **1982,** *65* (8), 104-111.

77. Lin, Y. S.; Tsai, T. H.; Hung, S. C.; Tien, S. W., Enhanced lithium electrochromism of atmospheric pressure plasma jet-synthesized tungsten/molybdenum oxide films for flexible electrochromic devices. *Journal of Solid State Electrochemistry* **2013,** *17* (4), 1077-1088.

78. Morales-Luna, M.; Arvizu, M. A.; Granqvist, C. G.; Niklasson, G. A., Electrochromic properties of W1-x-yNixTiyO3 thin films made by DC magnetron sputtering. *Thin Solid Films* **2016,** *615*, 292-299.

2 Uncovering Phase Transformation, Morphological Evolution, and Nanoscale Color Heterogeneity in Tungsten Oxide Electrochromic Materials

This chapter has been adapted from a published manuscript by Anyang Hu, Zhisen Jiang, Chunguang Kuai, Scott McGuigan, Dennis Nordlund, Yijin Liu and Feng Lin from the following reference: J. Mater. Chem. A, 2020, 8, 20000-20010 (DOI: 10.1039/d0ta06612e)
Reproduced with permission from the Royal Society of Chemistry.

2.1. Abstract

Controlling the electrochemical interfacial processes that govern the durability of electrochromic devices represents a key challenge in developing sustainable and cost-effective smart windows. Here, we revisit the classical tungsten trioxide (WO_3) materials as a platform to uncover the previously unknown interrelationship between phase transformation, morphological evolution, and nanoscale color heterogeneity in these materials. Through synchrotron/electron spectroscopic and imaging analyses, we report that the WO_3−electrolyte interface is influenced by the tungsten dissolution and redeposition during the electrochemical cycling. The tungsten redeposition provokes the in situ crystal growth, which ultimately leads to the phase transformation from the semicrystalline WO_3 to a nanoflake-shaped, proton-trapped tungsten trioxide dihydrate($H_xWO_3 \cdot 2H_2O$). The multidimensional quantification of the electronic structure reveals

that the tungsten reduction caused by the proton trapping is heterogeneous at the nanometric scale and is responsible for the nanoscale color heterogeneity. The interplay between phase transformation, morphological evolution, and nanoscale color heterogeneity results in degraded optical modulation, switching kinetics, Coulombic efficiency, and bleached-state transparency. Our results highlight that the high interfacial reactivity near the electrode surface may be the underlying mechanism for undesired bulk structural changes of electrochromic materials, and calls for fundamental studies in probing and controlling the electrode−electrolyte interfacial processes in electrochromic devices.

2.2. Introduction

The intercalation chemistry in inorganic solids has garnered increasing interest in recent years, primarily due to the controllable and reversible ion intercalation/deintercalation processes that can be operated in electrochromic devices[1] and rechargeable batteries.[2] Electrochromic devices can dynamically modulate electronic and optical properties on demand, providing a commercially viable approach for developing energy-saving technologies. Color tunability of electrochromic devices can be optimized using a novel design of materials and devices, including but not limited

to nanocrystal-in-glass composites exhibiting dual tunability of light,[3, 4] Fabry-Perot (F-P) nanocavity-type thin films showing full-spectrum tunability,[5] and pairing with solar cells to achieve self-sustainability.[6] Combining the reversible metal electrodeposition and ion intercalation chemistry, faster switching kinetics (~ one minute) has been demonstrated for inorganic metal oxide-based devices (with an area of 100 cm^2).[7] Nevertheless, the limited lifetime of electrochromic films in the acidic electrolyte during long-term electrochemical cycling still represents a daunting challenge towards the deep market penetration.[8, 9]

The performance degradation takes place ubiquitously in electrochromic films with various ion intercalation chemistries (e.g., H^+, Li^+, Na^+).[10] Tungsten oxide materials have maintained the prominent role in studying electrochromism even after decades of intensive research.[11-13] The ion intercalation into tungsten oxide, coupled with the charge compensating electrons, results in the formation of reduced blue colored tungsten bronzes with the formula M_xWO_3 (where M can be H^+, Li^+, and Na^+).[14] Researchers have used acidic (protonic) electrolytes since the early age of tungsten oxide electrochromism.[15] However, the poor WO_3 stability in the acidic environment has later shifted the research focus to non-protonic electrolytes, such as Li-ion electrolyte based on organic

carbonate solvents.[16] Unfortunately, the optical modulation and switching kinetics have been compromised due to the inferior Li^+ diffusion in metal oxide lattices[12, 17] and the performance degradation remains as a challenge in Li-ion electrolytes.[18, 19] Recent rejuvenation of the degraded electrochromic performance is achieved by applying a large constant current[1] or constant voltage.[20] Nevertheless, applying large current or voltage inevitably introduces side reactions at the electrode−electrolyte interface due to electrolyte decomposition.[21] Therefore, revealing the fundamental mechanism underlying the long-standing degradation challenge has become a critical task in the field. We believe that advanced characterization techniques, based on synchrotron X-ray spectroscopy and imaging, will provide a comprehensive platform to understand performance degradation.

The crystal structure, morphology, and charge distribution of the WO_3 material may evolve dynamically upon long-term electrochemical cycling. The phase transformation triggered by the cyclic ion intercalation/de-intercalation has been widely investigated.[22, 23] Monoclinic γ-WO_3 is the most stable phase at room temperature (298.15K),[24] but as the concentration of Li ions increases, the Li-intercalated phase gradually evolves from the monoclinic structure to a cubic

structure.[22] Moreover, the phase transformation can be observed at small scan rates over several electrochemical cycles.[25] On the other hand, the mass transport across the electrochemical interface during electrochemical cycling leads to dynamic speciation across the interface such as ion dissolution and redeposition, which will create a micro-environment for nanoscale morphological evolution. Furthermore, recent reports have demonstrated that the electrochemical reactions are highly heterogeneous at the electrode scale[26] as well as in the subdomains of an electrode,[27-29] resulting in significant charge heterogeneity. Phase transformations and morphological evolution may influence the local ion intercalation kinetics and further amplify the charge heterogeneity. Since the color of WO_3 films is directly related to its valence state, the charge heterogeneity in the electrochromic thin films observed during the electrochemical cycling will ultimately lead to color heterogeneity. To the best of our knowledge, there has not been a holistic study to investigate nanoscale color heterogeneity, phase transformation, and morphological evolution in electrochromic materials or to establish the relationship between these phenomena and the lifetime of electrochromic thin films.

Herein, combining electrochemical diagnostics with synchrotron/electron spectroscopic and imaging analyses, we unravel the interrelationship between nanoscale color heterogeneity, phase transformation, morphological evolution, and performance degradation in classical proton-intercalating WO_3 electrochromic materials among long-term electrochemical cycling. We discover that tungsten dissolution/redeposition and irreversible trapping of intercalating ions in the lattice, as two highly correlated degradation mechanisms, collectively contribute to the drastic morphological evolution and degradation of the WO_3 materials. As a result, these changes undermine the optical modulation, Coulombic efficiency, switching kinetics, and lifetime of the electrochromic thin films. With the knowledge from these diagnostic studies, our results provide insights into improving the stability of metal oxide electrodes in acidic aqueous electrolytes.

2.3. Materials and methods

2.3.1. Synthesis of WO_3 electrochromic thin film

Triblock copolymer Pluronic P123 (poly (ethylene glycol)-block-poly (propylene glycol)-block-poly (ethylene glycol), $EO_{20}PO_{70}EO_{20}$, Sigma-Aldrich), tungsten (VI) chloride WCl_6 (Acros

Organics), and anhydrous ethanol (Decon Labs, Inc.) were used without further purification. As previously reported[30], 2.0 g of Pluronic P123 was dissolved in 10 g (12.67 ml) of anhydrous ethanol by sonication for 20 minutes. 0.003 moles tungsten (VI) chloride was then added and stirred for 15 h in the fume hood to prepare the solution for spraying. Thin films were then spray-coated onto electron conductive fluorine-doped tin oxide (FTO) glass substrates (MSE Supplies LLC.) by using an Airbrushing system (Master Airbrush). The spray pressure and distance were 20 psi and 20 cm, respectively. The hydrolysis of the sprayed film was performed in the atmosphere of a saturated NaCl(aq.) for 15 h. The collected thin films were calcinated in a box furnace at 350 °C with a ramp rate 1°C/min, hold at 350 °C for 120 minutes, and naturally cooled down to room temperature.

2.3.2. Electrochemical measurement

All electrochemical performance was measured in a three-electrode configuration with the 0.5 M sulfuric acid (H_2SO_4) as the liquid electrolyte, the platinum foil as the counter electrode, and the saturated calomel electrode (Hg/Hg_2Cl_2 in saturated KCl solution, SCE) as the reference

electrode. Cyclic voltammetry (CV) was performed by using a potentiostat (SP-150, BioLogic, France) with a voltage range of -0.2–0.6 V vs. SCE. Switching kinetics was measured using chronoamperometry (CA) cycling between -0.2 to 0.6 V vs. SCE., where each potential was held for 40 seconds. Switching speed is defined as the time needed to achieve ∼90% of transmittance change under each potential. The transmittance difference between the bleached state and the colored state is typically defined as optical modulation.

2.3.3. *In situ* UV-vis measurement

In-situ optical transmission with a wide wavelength range (450-950 nm) was measured by an Ocean Optics spectrometer. An optical glass cell was used as the *in-situ* electrochemical cell. The WO_3 thin film on FTO was placed in the center of the laser path. A potentiostat (SP-150, BioLogic, France) was used for the electrochemical measurement. A three-electrode configuration was used, where the WO_3 thin film on FTO serves as the working electrode, a platinum wire is the counter electrode, and the saturated calomel electrode is the reference electrode.

2.3.4. Materials characterization

The morphology of thin films was characterized on LEO 1550 field-emission scanning electron microscopy (SEM) with an accelerating voltage of 5 kV and JEOL 2100 transmission electron microscope (TEM) with a 200 kV acceleration voltage. To increase the electronic conductivity, a 7-nm-thick Au/Pd coating layer was deposited on the film surface with a Cressington 208 sputter before conducting SEM. The EDS results were conducted with the SEM with an accelerating voltage of 20 kV. The samples for TEM were carefully scratched off the FTO substrate and fully sonicated with IPA and dropped onto copper grids. The film thickness was measured by Dektax 150 surface profilometer (Veeco) using contact profilometry techniques. The X-ray powder diffraction was acquired through scratching 10 pieces of thin films on a Rigaku MiniFlex II diffractometer with a Cu Kα X-ray radiation (λ = 1.54 Å). The thin-film material was gently scratched off the FTO substrate to avoid the interrupting signals of FTO in XRD. Data collection was performed with 10° to 90° as 2θ range, 0.02° as step size, and 0.2° per minute as scan rate. The concentration of dissolved tungsten ions was analyzed using a Thermo Electron iCAP-RQ inductively coupled plasma mass spectrometer (ICP-MS). Samples and W calibration

standards were diluted to a mixture with 2% nitric acid by volume. X-ray photoelectron spectroscopy (XPS) characterization was performed on a PHI VersaProbe III scanning XPS microscope using a monochromatic Al K-alpha X-ray source (1486.6 eV). XPS Spectra were acquired with 200 μm/50 W/15 kV X-ray settings and dual beam charge neutralization. The C-C peak at 284.8 eV was used as the reference for all binding energies. Atomic concentration % of elements were determined based on the integrated intensity of the elemental photoemission features with the correction by relative atomic sensitivity factors. Analysis of XPS data was performed based on a 2.18 eV $W4f_{7/2}$–$W4f_{5/2}$ spin-orbit separation. Soft XAS measurements were performed on the 31-pole wiggler beamline 10-1 at Stanford Synchrotron Radiation Light source (SSRL, SLAC National Accelerator Laboratory) using a ring current of 350 mA and a 1000 L mm^{-1} spherical grating monochromator with 20 μm entrance and exit slits, providing $\sim 10^{11}$ ph s^{-1} at 0.2 eV resolution in a 1 mm^2 beam spot. Data collection was conducted under ultrahigh vacuum (10^{-9} Torr) in a single load at room temperature using total electron yield (TEY). The sample drain current was mainly collected. All spectra were normalized by the current from freshly evaporated gold on a fine grid positioned upstream of the main chamber. After thin films were cycled to the

designated number of cycles, they were rinsed with IPA and dried with high-pressure N_2 gas, immediately transferred to an Ar-filled glove box with water level and oxygen level both less than 0.5 ppm and then they (with the FTO substrate) were cut into small pieces and fixed to an aluminum holder using conductive carbon tape and protected in the glove box for the XAS characterization. Similarly, some cycled thin film samples were also sealed in aluminum bags in the glove box, and they were gently scratched off the FTO substrate by the doctor blade and sealed into quartz capillary tubes using epoxy glue for the Transmission X-ray microscopy (TXM) characterization. The TXM was performed at beamline 6-2c at SSRL. A home-developed software named as TXM-Wizard was used to analyze all the tomography results.[31] The TXM analysis is based on the sample directly scratched from the WO_3 film and the scattered nanoparticles in the vicinity of these large scratched WO_3 film samples are not used for the TXM quantification due to the lack of spatial resolution for these nanoparticles. Specifically, the XANES spectrum of each pixel is created by imposing and aligning the absorption spectra at various energies. After the normalization procedure (**Fig. S1**), the pre-edge intensity of the spectra is set to be zero and the post-edge intensity is set to be one. To quantify the relative energy shift of the XANES spectra,

the white-line (peak) energy is extracted to benchmark the relative valence state of W (a proxy for the local state of charge) through the data processing in MATLAB. Eventually, the white-line energy distribution is used to generate the color maps showing the valence state distribution.

2.4. Results and discussion

2.4.1. Evolution of chemical composition, crystal structure, and morphology upon long-term electrochemical cycling

The ion-intercalation/deintercalation initiates at the interface between the electrode and the electrolyte and advances towards the bulk lattice through solid-state diffusion.[29] The ion-intercalation kinetics is mainly influenced by the morphology and crystal structure of the electrode material, which determines the ion diffusion length and the occupying sites of intercalated ions, respectively.[12] Therefore, the durability of the electrochemical performance heavily relies on the stability of the nanoscale morphology and crystal structure of the electrode material.

Here, we first investigate the stability of electrochemical performance during long-term cyclic voltammetry (CV) measurements. We can observe the degradation during 3,000 CV cycles, with

the gradual shrinkage of the cathodic and anodic features (**Fig. 1a)**. A remarkable trend of morphology evolution is observed during the long-term CV measurements (**Fig. 1b-1f**). The pristine WO_3 thin film does not exhibit any defined nanostructure, similar to our previous study.[32, 33] However, as the cycle number increases, there is a clear formation of nanoflakes, and the size and surface coverage of nanoflakes also correspondingly increase. Back to 1990, Gavrilko and Stepkin found that storing amorphous tungsten trioxide in 0.2 M H_2SO_4 electrolyte may provoke the formation of tungsten trioxide hydrate crystals.[34] To the best of our knowledge, however, the morphological evolution under electrochemical cycling has been rarely reported. Albeit potentially important, this phenomenon has not been sufficiently considered in most tungsten oxide electrochemical studies.[30, 35, 36] The entire film evolves into nanoflakes after 3,000 cycles, as shown in the cross-sectional images (**Fig. 1g** and **1h**). Such drastic morphological evolution is usually associated with changes in the local chemical bonding and crystal structure of the material, suggesting that the chemical composition of our films may have been altered.[37] Therefore, X-ray diffraction (XRD) and transmission electron microscopy (TEM) are collectively utilized to characterize and identify the crystal structure before and after the long-term electrochemical

cycling. The XRD patterns of pristine and cycled thin films are shown in **Fig. 1i** and **1j**, respectively. The diffraction peaks of the pristine film match well with those of the monoclinic WO_3, which have the following lattice constants: a=7.301Å, b=7.539Å, c=7.689Å, α=90°, β=90.89°, and γ=90° (PDF # 83-0951). However, due to its low crystallinity, the diffraction peaks of the pristine film are not sharp and it is difficult to individualize each peak, which is a characteristic of WO_3 thin films synthesized using the sol-gel chemistry and low-temperature calcination.[30, 32] The pristine WO_3 thin film consists of ~5 nm WO_3 nanocrystals embedded in the amorphous WO_3 matrix (**Fig. 1k**). These nanocrystals evolve into large nanoflakes after the long-term electrochemical cycling (**Fig.1l**). The fast Fourier transform (FFT) images of two sets of lattice fringes show d spacings of 0.377 nm and 0.365 nm (**Fig. 1k**), corresponding to the (020) and (200) planes of the monoclinic WO_3, individually. After the long-term cycling, the material exhibits single-crystal characteristics with continuous lattice fringes and a 0.370 nm d-spacing (**Fig. 1l**), which corresponds to the (100) peak in the XRD pattern (**Fig. 1j**). Furthermore, the chemical composition of the nanoflakes is proposed to be close to $H_{0.12}WO_3 \cdot 2H_2O$ [PDF# 40-0693]. However, the exact chemical composition remains unclear because XRD is not sensitive to the

minor variation of proton concentration in tungsten oxide hydrates. As shown by the SEM images (**Fig. 1b-1f**), the nanoflakes typically have diameters of 300-400 nm and thicknesses of 10-30 nm, suggesting that the nanoflake growth is anisotropic. The directional addition of precursor to the nuclei attempts to minimize the most energetically unfavorable facet by growing rapidly in the direction perpendicular to the corresponding facet.[38] These precursors are found to be the dissolved W species, as discussed later in this paper.

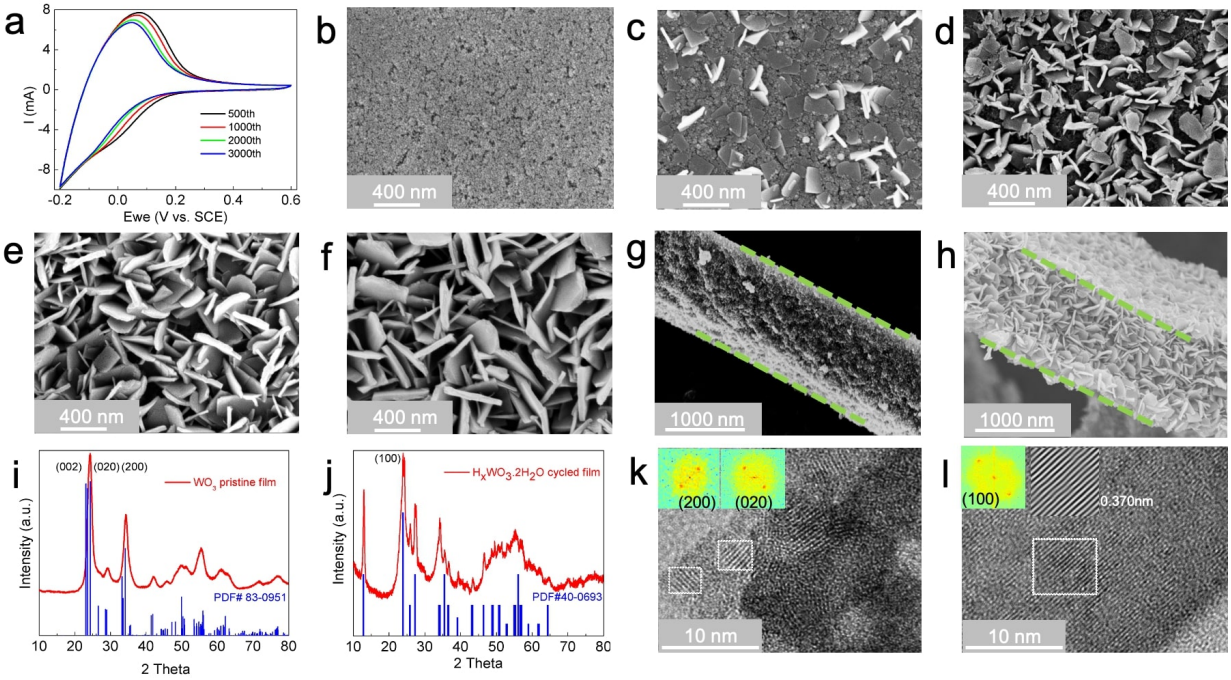

Fig. 4 The evolution of chemical composition, crystal structure, and morphology during long-term electrochemical cycling. (a) 3,000 CV cycles of the WO_3 thin film in 0.5M H_2SO_4 (aq.) at 60mV/s within -0.2V-0.6V vs. SCE., where the degradation along the 500th, 1,000th, 2,000th, and

3,000th cycles can be observed. A WO_3 film with a thickness of about 1,000 nm was used for the test. The morphology measured by SEM: (b) in the pristine state, (c) after 500 CV cycles, (d) after 1,000 CV cycles, (e) after 2,000 CV cycles, and (f) after 3,000 CV cycles, where the morphology gradually evolves to nanoflakes. A WO_3 film with a thickness of about 1,000 nm was equally cut into five pieces for the tests (b)-(f). The cross-section SEM images of (g) the pristine film and (h) the film after 3,000 CV cycles, where the dashed lines are made to illustrate the thickness. The film thickness is close to 1,000 nm. (i) The XRD pattern of the pristine film (WO_3, PDF# 83-0951) and (j) The XRD pattern of the film after 3,000 CV cycles ($H_xWO_3 \cdot 2H_2O$, PDF# 40-0693). (k) HRTEM image of the pristine film that consists of WO_3 nanocrystals embedded in the amorphous WO_3 matrix, where the inserted images show the FFT patterns of the selected regions labeled in the HRTEM image. (l) HRTEM image of a $H_xWO_3 \cdot 2H_2O$ nanoflake, where the inserted images are the FFT pattern of the whole HRTEM image and the Inverse Fast Fourier Transform (IFFT) pattern of the selected region labeled in the HRTEM image.

The evolution of crystal structure and chemical composition may be associated with the drastic morphological change upon electrochemical cycling. To our knowledge, the direct evolution from

tungsten trioxide to the proton-trapped tungsten trioxide dihydrate is rarely reported in electrochemical devices. We hypothesize that the performance degradation of WO_3 thin films cycled in the acidic electrolyte is associated with morphological evolution. Therefore, we establish a systematic study to investigate the underlying mechanism for the morphological evolution. Specifically, we propose that the evolution of chemical composition, crystal structure, and morphology are all related to the dissolution/redeposition of W species and proton trapping in the lattice. We test our hypothesis through (1) manipulating the concentration of W species in the electrolyte to control the formation of nanoflakes, as well as studying the differences in electrochemical and optical properties with varying degrees of nanoflake formation; and (2) investigating the effects of proton trapping in the WO_3 lattice on the W valence state, as well as probing the evolution of the nanoscale color (charge) heterogeneity during the long-term electrochemical cycling.

2.4.2. Impact of the dissolution and redeposition of tungsten species on the morphological evolution

In order to evaluate the dissolution/redeposition behavior of WO_3 thin films in the acidic electrolyte, we tailor the concentration of W ions in the electrolyte by (1) reducing the concentration of W species in the electrolyte utilizing an electrochemical flow cell (the schematic set-up is shown in **Fig. 2a**), and (2) increasing the concentration of W species through adding 0.1 mM WCl_6 into the 0.5 M H_2SO_4 electrolyte. The concentration of dissolved W species in the electrolyte (starting from 0.5 M H_2SO_4) throughout 3,000 CV cycles is quantified using the inductively coupled plasma mass spectrometry (ICP-MS) measurements (**Fig. 2b**). The concentration of dissolved W species in the electrolyte increases to ~27 μM (after 1,000 cycles) and then to ~36 μM (after 3,000 cycles). This observation is consistent with a previous study that performance degradation may be related to the film dissolution.[39] Furthermore, based on the Pourbaix diagram of tungsten in aqueous solution, WO_3 is not the most thermodynamically stable compound in the acidic electrolyte with a pH value close to 0 and a potential close to 0 V (vs. SHE, Standard Hydrogen Electrode).[40,41] The chemical composition of the dissolved W species may vary with the local pH gradient at the electrode–electrolyte interface.[42] The initial pH value of the electrolyte is ~0.3 and the pH slightly increases during the long-term electrochemical cycling due

to the consumption of protons. The dissolved W species can be tungstate ion (e.g., WO_4^{2-}) in the basic solution or polytungstate ions (e.g., HWO_4^-, $HW_6O_{21}^{5-}$, $H_2W_{12}O_{42}^{10-}$) in the acidic solution.[39, 40] Therefore, during the ion intercalation (discharging) process, protons or hydroniums are driven toward the electrode–electrolyte interface, while the polytungstate ions are driven away from the interface. The ion deintercalation (charging) process shows the opposite mass transfer. These soluble polytungstate ions may react with water or hydronium to form thermodynamically stable species such as tungsten trioxide dihydrate $WO_3 \cdot 2H_2O$, which can precipitate out in the acidic electrolyte with the increasing concentration of soluble polytungstate ions at the electrode–electrolyte interface.[40]

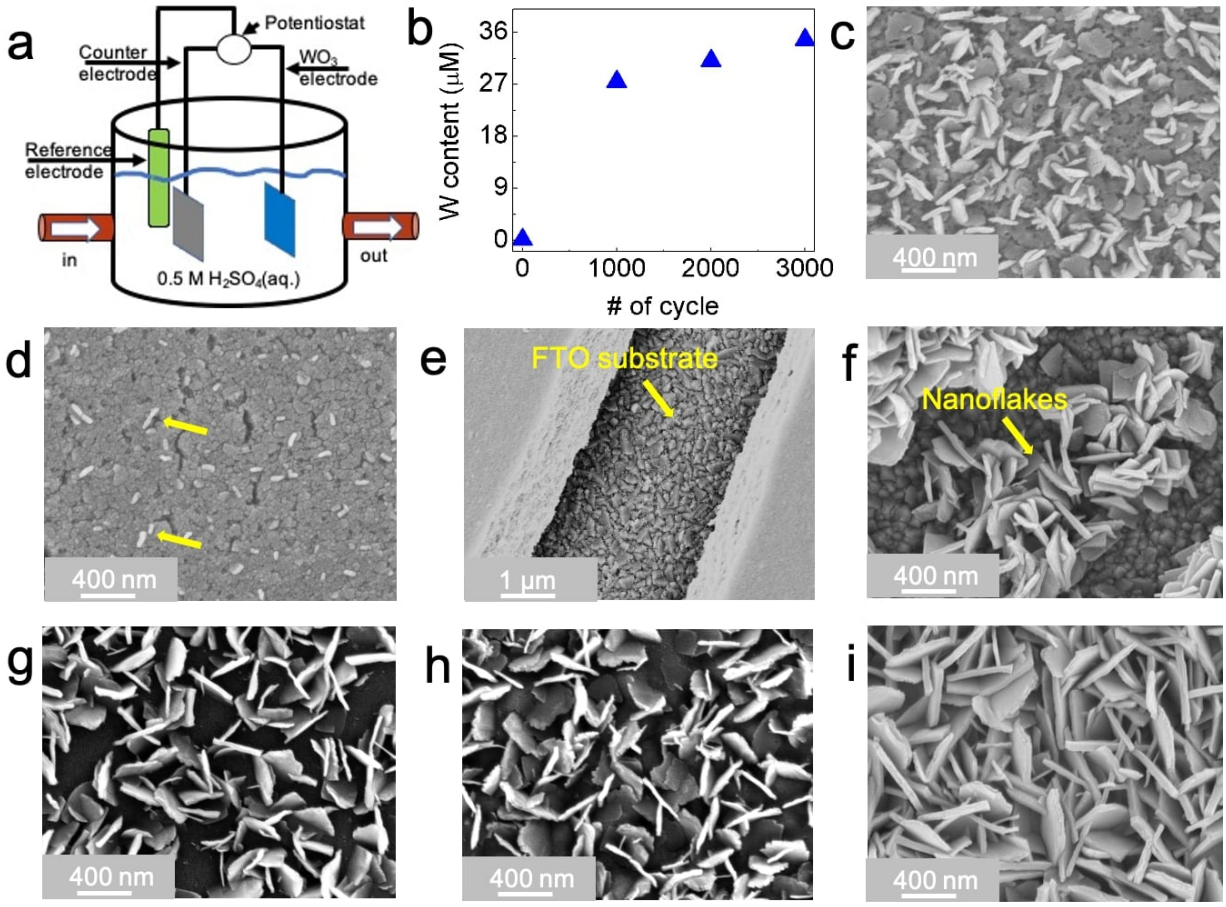

Fig. 2 Metal oxide film dissolution and redeposition during the long-term electrochemical cycling. (a) The schematic set-up of the electrochemical flow cell with a three-electrode configuration, where the concentration of dissolved W species remains minimal in the electrolyte due to the constant replenishment of fresh electrolyte. (b) The concentration of dissolved W species in the electrolyte vs. cycle number during 3,000 CV cycles in the regular electrochemical cell. (c) The formation of nanoflakes in the regular electrochemical cell after 3,000 CV cycles in 0.5 M H_2SO_4(aq.) at 60 mV/s with -0.2V-0.6V vs. SCE. (d) Decreased formation of nanoflakes in the

flow cell after 3,000 CV cycles in 0.5 M H_2SO_4(aq.) at 60 mV/s with -0.2V-0.6V vs. SCE. The pump-in and pump-out rates are both set as 1.35 ml/min. A WO_3 film with a thickness of about 700 nm was equally cut into two pieces for the tests in (c)-(d). (e) The pristine film with a clean crack showing pure FTO substrate. (f) The cycled film with nanoflake deposition in the crack after 3,000 CV cycles in the regular cell. (g) The formation of nanoflakes in the regular electrochemical cell after the first 2,000 CV cycles in 0.5 M H_2SO_4(aq.) at 60 mV/s with -0.2V-0.6V vs. SCE. (h) Increased degree of nanoflake formation in the regular electrochemical cell after total 3,000 CV cycles in 0.5 M H_2SO_4(aq.) at 60 mV/s with -0.2V-0.6V vs. SCE. (i) The largest degree of nanoflake formation in the regular electrochemical cell after total 3,000 CV cycles in 0.1 mM WCl_6 (aq.) + 0.5 M H_2SO_4(aq.) at 60 mV/s with -0.2V-0.6V vs. SCE. A WO_3 film with a thickness of ~1,000 nm was equally cut into three pieces for the tests in (g)-(i).

Regarding the characteristic nanostructure, tungsten trioxide dihydrates with nanoflake morphology have been widely synthesized by hydrothermal methods.[43,44] However, the transformation of tungsten trioxide nanocrystals to tungsten trioxide hydrate nanoflakes is rarely reported in electrochromic devices or other electrochemical devices. Considering the dissolution

and redeposition hypothesis, using electrochemical flow cell can minimize the concentration of dissolved W species in the electrolyte. The observed morphological evolution is completely different between the regular cell and the flow cell (**Fig. 2c and 2d**). After the long-term electrochemical cycling, the amount of nanoflakes found in the flow cell is less than that of using the regular cell. The adhesion between the FTO substrate and these redeposited nanoflakes is strong enough to resist such a marginal disturbance of the electrolyte flow (**Fig. S2**). Therefore, the possibility that nanoflakes will flow into the electrolyte in the flow cell is quite low. These results support that the redeposition of dissolved W species in the electrolyte is responsible for the nanoflake formation. A lower concentration of dissolved W species results in a lower likelihood of redeposition and thus less nanoflake formation. Moreover, we observe the direct nanoflake formation on the cracked region (exposed FTO surface) after the long-term electrochemical cycling in the regular cell (**Fig. 2e**, **2f**, and **S3**). The nanoflake can directly grow on fresh FTO without a seed layer which is typically needed in the hydrothermal synthesis.[43] Increasing content of W element can be detected in the cracked region with nanoflake formation after cycling (**Table S1**). Furthermore, deliberately increasing the concentration of W species in the original electrolyte

causes more redeposition after cycling, which results in the more significant formation of nanoflakes, as shown by the SEM results (**Fig. 2g-2i**). Collectively, our results indicate that the accumulative speciation at the electrode–electrolyte interface through repeated dissolution/redeposition is a dominating factor for the nanoflake formation and that electrochemical degradation is likely associated with the dissolution-induced loss of active material and morphological evolution (more discussion later).

2.4.3. Visualizing the development of nanoscale color heterogeneity

In the tungsten oxide or tungsten oxide hydrate lattices, the proton trapping upon extended cycling can result in the irreversible electrochemical reduction of tungsten cations in the lattice. Therefore, to test our hypothesis about the ion trapping in the lattice, we perform a range of spectroscopic and imaging characterizations at multiple scales. The surface characterizations are based on the O K-edge soft X-ray absorption spectroscopy (soft XAS) and W4f X-ray photoelectron spectroscopy (XPS). The bulk characterization, especially the visualization of the electronic states in two dimensions (2D) is based on the W L_3-edge transmission X-ray microscopy

(TXM). During the discharge process, when protons diffuse into the interstitial sites of the WO_6 octahedra, the W valence state is decreased. The W valence state then increases when protons leave interstitial sites under the charging process.[45] However, the charge/discharge irreversibility (i.e., Coulombic inefficiency) can lead to the accumulation of intercalating ions in the lattice, resulting in the irreversible W reduction.

The soft XAS in the total electron yield (TEY) mode has a probing depth of 5-10 nm.[46] The pre-edge at 530 eV of the O K-edge XAS represents the hybridization between W5d orbitals and O2p orbitals.[47,48] The pre-edge intensity is noticeably changed after the long-term electrochemical cycling (**Fig. 3a**), indicating the changes in the local W−O bonding environment (likely the W reduction). There are other changes in the O K-edge XAS, which may be associated with the local structural changes due to the phase transformation identified in **Fig. 1i** and **1j**. The tungsten reduction is further confirmed by the direct characterization of the W valence state using the surface sensitive W4f XPS (**Fig. 3b)**. Two peaks centered at 36.1 and 38.1 eV are assigned to W^{6+}, while the peaks located at 34.5 and 37.2 eV are assigned to W^{5+}.[49,50] We only deconvolute the W4f spectra to W^{6+} and W^{5+}. However, it should be noted that from the spectroscopy standpoint, W^{5+}

is considered as the linear combination product of W^{6+} with a lower W valence state. In summary, there is a clear reduction of W after long-term cycling (**Table S2)**.

We then perform TXM to visualize the distribution of W valence state in the electrochromic film after different cycle numbers. Through measuring the spatially resolved X-ray absorption spectra at W L_3-edge,[51,52] TXM is capable of probing the local valence state change with a nominal spatial resolution of around 30 nm.[31, 53, 54] As we featured, the macroscopic change in the color of the electrochromic film is caused by the change of W valence states,[35] therefore, the tungsten valence state distribution can be used to represent the color distribution at the nanoscale. We first perform 2D TXM mapping on the electrochromic film in the bleached state after various cycle numbers: pristine film (**Fig. 3c**), after 600 CV cycles (**Fig. 3d**), after 1,500 CV cycles (**Fig. 3e**), after 2,000 CV cycles(**Fig. 3f**), and after 3,000 CV cycles **(Fig. 3g)**. Then the corresponding histograms of each energy distribution are shown in **Fig. 3h**. The center of the histogram gradually shifts to lower energy as the cycle number increases. Therefore, there is a continuous reduction of W during the 3,000 cycles, which is consistent with soft XAS, XPS, and the formation of $H_xWO_3 \cdot 2H_2O$ nanoflakes discussed above. Conjointly, our multiscale surface-to-bulk

characterization reveals that the ion trapping takes place at all length scales, leading to W reduction throughout the thin film.

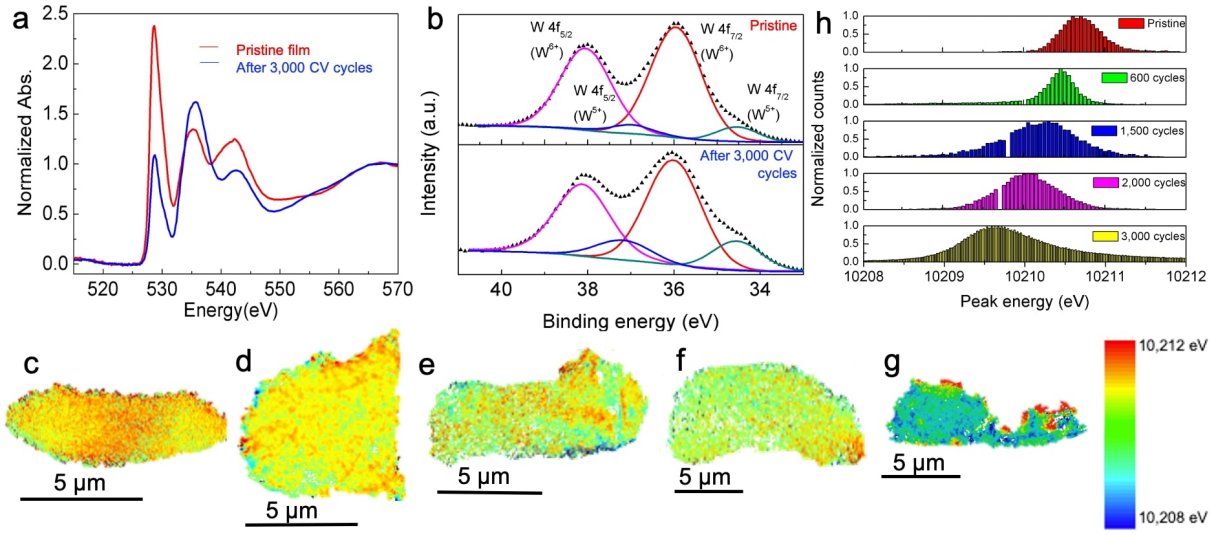

Fig.3 Probing the W reduction and nanoscale color (charge) heterogeneity induced by proton trapping. (a) O K-edge XAS (TEY mode) of the pristine film and the cycled film in the bleached state (after 3,000 CV cycles). (b) The W 4f XPS spectra of the pristine film and the cycled film in the bleached state (after 3,000 CV cycles). W valence state sensitive 2D TXM images of (c) pristine, (d) after 600 CV cycles, (e) after 1,500 CV cycles, (f) after 2,000 CV cycles, and (g) after 3,000 CV cycles. Each TXM image represents a WO_3 thin film fragment, which is peeled off from its original FTO substrate. The relative valence state is represented by the W L_3-edge white-line energy displayed by the color bar to the right, where higher white-line energy represents a higher

W valence state. (h) The W L_3-edge white-line energy distribution along with the increase of the total cycling numbers. O K-edge XAS, XPS, and TXM provide a holistic view that the overall W valence state is decreased at multiple length scales. The color (charge) heterogeneity increases upon electrochemical cycling.

From the TXM mapping, we have discovered that the W valence state distribution exhibits a discernible degree of heterogeneity for all the films, which also signifies the nanoscale color heterogeneity present in these films. To the best of our knowledge, we are not aware of any study reporting the nanoscale color heterogeneity in inorganic electrochromic films. The color heterogeneity has been reported and explained at length scales different from our current study. In practical large-scale devices, the color heterogeneity sometimes can be caused by the non-uniform distribution of the electric field (i.e., the conductivity difference), which has been widely seen in commercial smart windows during the coloration process. On the single-crystal level, the heterogeneous particle-particle interactions also cause non-uniform coloration.[55] However, our results demonstrate a distinct mechanism for the nanoscale color heterogeneity, which is originated from the morphological evolution and phase transformation. Our results will shed light on

understanding the degradation mechanism of WO_3-based materials in the protonic electrolyte as well as informing the future design of advanced electrochromic devices. First, the development of color heterogeneity may be originated from the non-uniform ion trapping across the thin film. The W L_3-edge white-line energy distribution becomes broader as the cycle number increases, which indicates that the nanoscale charge heterogeneity is exacerbated with increasing cycle number, so does the color heterogeneity (**Fig. 3h**). Second, the nanoscale charge heterogeneity caused by ion-trapping may result in different lattice volume changes between neighboring domains thus creating local mechanical stress and leading to chemomechanical breakdown.[56] Third, the chemomechanical breakdown, expressed as the microcrack formation, may expose more surface to the electrolyte and accelerate the dissolution of W species into the electrolyte, allowing for the further redeposition and growth of nanoflakes. Fourth, the accumulation of the reduced W species in the nanoflakes will lead to the reduced transmittance in the bleached state. Last but not least, the electrochromic performance metrics, such as switching kinetics and optical modulation, may show a strong correlation with nanoscale color heterogeneity, phase transformation, and morphological evolution (more discussion later).

2.4.4. Evolution of electrochromic performance upon long-term cycling

As hypothesized above, we believe that the performance degradation is likely associated with (1) the WO_3 thin film dissolution and redeposition as tungsten trioxide dihydrate ($WO_3 \cdot 2H_2O$), and (2) the proton trapping caused by the irreversible ion intercalation/deintercalation in the crystal lattice ($H_xWO_3 \cdot 2H_2O$), resulting in the irreversible W reduction (**Fig. 3**). Here, we combine electrochemical and optical measurements to understand the contribution of these factors to performance degradation. Two sets of control experiments are used: (1) the WO_3 thin film showing nanoflake formation in the regular cell (**Fig. 4a** and **4b**); and (2) the WO_3 thin film showing minimal morphological evolution in the flow cell (**Fig. 4c** and **4d**).

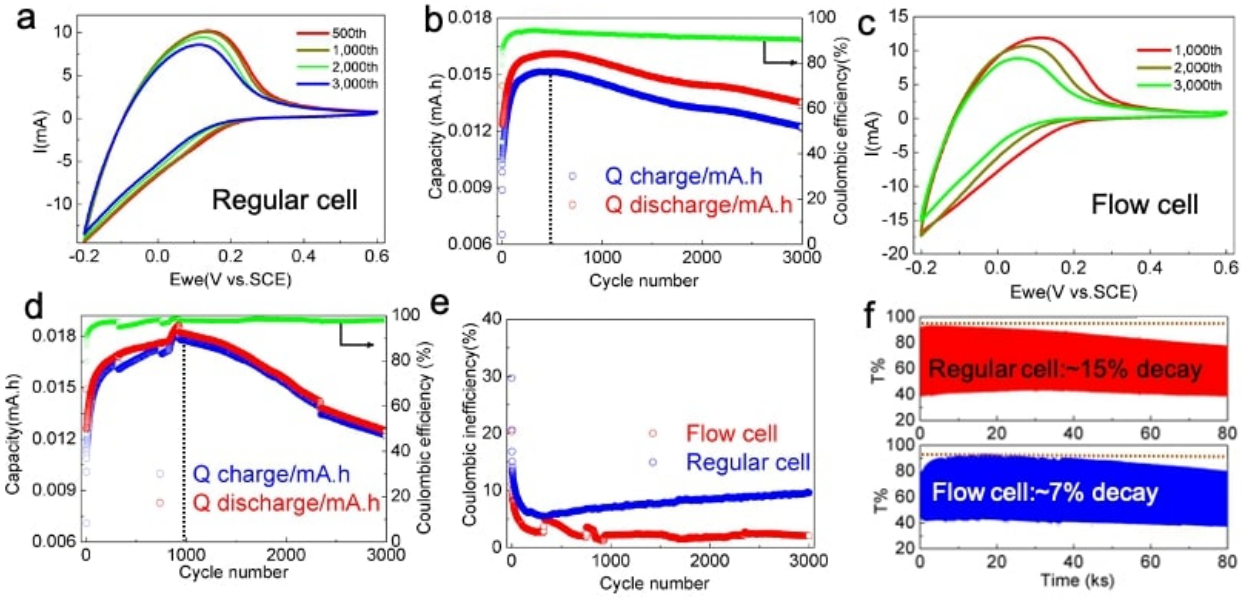

Fig.4 The electrochromic performance is largely influenced by the morphology evolution. (a) 3,000 CV cycles of a pristine WO_3 thin film (with a thickness of ~1,000 nm) in 0.5M H_2SO_4(aq.) at 60mV/s with -0.2V-0.6V vs. SCE. in the regular cell. (b) The corresponding charge and discharge capacity and their ratio (Coulombic efficiency) under 3,000 CV cycles of WO_3 thin film in the regular cell. The dotted line indicates that the capacity reaches the maximum after the initial activation period. (c) 3,000 CV cycles of a pristine WO_3 thin film (with a thickness of ~1,000 nm) in 0.5M H_2SO_4(aq.) at 60mV/s with -0.2V-0.6V vs. SCE. in the flow cell. (d) The corresponding charge and discharge capacity and their ratio (Coulombic efficiency) under 3,000 CV cycles of WO_3 thin film in the flow cell. The dotted line indicates that the capacity reaches the maximum after the initial activation period. (e) The comparison of Coulombic inefficiency (mostly

contributed by the ion-trapping) in each CV cycle between the regular cell and the flow cell. (f) The in-situ transmittance at 600 nm of two pristine WO_3 thin films under the same 3,000 CV cycles in the regular cell and the flow cell, respectively.

Through comparing the CV measurements in **Fig. 4a** and **4c**, we find that the degradation takes place in both electrochemical cells. As shown in **Fig. 4b** and **4d**, performance degradation in the regular cell starts from around the 500th cycle. There is an activation period, where a number of initial cycles are required to reduce the charge transfer impedance before obtaining the maximum charge capacity,[57, 58] and subsequently, the charge and discharge capacity gradually decreases. However, the performance degradation in the flow cell begins around the 1,000th cycle, and the decrease in the charge and discharge capacity is more pronounced afterward. With the continuous replenishment of the fresh electrolyte and the removal of the used electrolyte, the active material is dissolved more significantly in the flow cell, thus the degradation of the peak currents becomes greater (**Fig. 4c**). This is direct evidence that the W dissolution results in performance degradation during long-term cycling. The degradation in the flow cell is faster than the regular

cell in terms of tungsten oxide dissolution. The continuous flowing of fresh electrolytes will accelerate the loss of tungsten species.

In general, the discharge capacity (ion intercalation) is larger than the charge capacity (ion deintercalation) in both electrochemical cells. However, the Coulombic efficiency (charge capacity/discharge capacity) varies greatly in these electrochemical cells. The Coulombic efficiency of the regular cell is around 90%, while the Coulombic efficiency of the flow cell approaches 98%. In other words, with increasing cycle number, the Coulombic inefficiency (which mostly contributes to the ion-trapping ratio) in each cycle of the regular cell approaches 10%, whereas it is suppressed to about 2% in the flow cell (**Fig. 4e)**. These results suggest that most ion-trapping phenomenon takes place synchronously with the formation of nanoflakes and that the film with more profound nanoflake formation has more ions trapped inside the lattice thus leading to lower W valence states, as discussed in **Fig. 3**. The proton trapping is likely due to the fact that protons prefer to form hydroxyl groups with the oxygen atom in the lattice.[59]

The apparent diffusion coefficient gradually decreases during the long-term electrochemical cycling calculated using the Randles–Sevcik equation (**Fig. S4, S5,** and **Table S3**), which

coincides with the gradual phase transformation and morphological evolution from tungsten trioxide (small nanocrystals) to tungsten trioxide dihydrate (large nanoflakes). The ion kinetics can also be studied through measuring the switching speed (such as coloration time and bleaching time), which is usually measured by using chronoamperometry (CA), and its evolution can be obtained between different numbers of CV cycles (**Fig. S6)**. The coloration time increases from 5.2 seconds to 6.6 seconds, and the bleaching time increases from 1.5 seconds to 3.1 seconds (**Fig. S7**). In the meantime, the optical modulation gradually decreases from 60% to 45% from the 500th to 3,000th cycle, with the major contribution of decaying transmittance in the bleached state originating from the increasingly reduced W (**Fig. S6)**. Collectively, the apparent diffusion coefficient and switching kinetics measurements show that the ion kinetics is impeded due to the phase transformation and morphological evolution. The intercalated protons preferably bond to bridging oxygen atoms and form hydroxyl groups in the lattice.[60] However, the presence of O-H bonds indicates that the solid-state diffusion is relatively low,[59] some intercalated protons may become partially immobile due to trapping sites having higher energy barriers.[1] Therefore, considering the gradual phase transformation from WO_3 to $H_xWO_3 \cdot 2H_2O$ during the long-term

electrochemical cycling, the possibility of having more sites with higher energy barrier is correspondingly increased, and that the solid-state diffusion becomes more obstructed.

The ion-trapping coupled with phase transformation and morphological evolution also imposes a profound impact on the long-term optical performance. As shown in **Fig. 4f**, after 3,000 CV cycles, the optical modulation of the regular cell decreases by 15%, which is more significant than that of the flow cell (7% decrease). Having only 7% of degradation is quite impressive for the flow cell since there is a large loss of active material due to the constant removal of the used electrolyte. The suppressed formation of nanoflakes and limited ion-trapping behaviors may help stabilize the electrochromic performance of the WO_3 electrode in acidic electrolytes.

The electrochromic measurements suggest that the morphological evolution induced by the dissolution/redeposition and ion-trapping impedes the proton transport kinetics, slows down the switching kinetics, and degrades the optical modulation during long-term cycling.

2.5. Conclusion

In summary, we establish the interrelationship between morphological evolution, phase transformation, nanoscale charge distribution, and performance degradation in a classical ion-intercalating tungsten oxide electrochromic material. We experimentally reveal that tungsten dissolution/redeposition and ion-trapping are the two fundamental origins responsible for performance degradation during long-term cycling, such as impeded switching kinetics and faded optical modulation. Through synchrotron spectroscopic and microscopic characterizations, we have discovered that the phase transformation from tungsten trioxide to proton-trapped tungsten trioxide dihydrate promotes the morphological change from small nanocrystals to large nanoflakes. We highlight that the morphological evolution is influenced by multiple factors, such as film thickness, electrolyte concentration, charging rate, and dissolved tungsten species concentration at the electrode–electrolyte interface. We will report the results in a separate study. Furthermore, the charge heterogeneity of the thin film is consistent with the phase transformation during the long-term electrochemical cycling, and a significant degree of nanoscale color heterogeneity is induced by the charge heterogeneity. We believe that our study can provide some critical insights into

understanding and improving inorganic electrochromism. First, the phase transformation provides insights into the ion diffusion kinetics involving the ion intercalation chemistry in metal oxides and metal oxide hydrates. Second, the nanoscale color heterogeneity may explain the spatially non-uniform electrochromic processes. Future studies may focus on understanding how the color (charge) heterogeneity contributes to the local mechanical stress buildup and thus the performance fading. Third, many reported strategies on improving the electrochromic performance, such as elemental doping[61] and surface coating,[62] may have grounded on the mechanistic processes reported in this study, which is to inhibit the electrode dissolution. Last but not least, the overwhelming morphological changes reported here may raise some concerns on the legitimacy of the studies that attribute the electrochromic performance solely to a certain initial nanostructure. More efforts are needed to investigate the multiscale changes of electrochromic materials during long-term cycling. Finally, we believe that the entire degradation process may initiate at the electrode−electrolyte interface, thus more studies are needed to probe and control the interfacial chemistry in electrochromic and other electrochemical devices.

2.6. Supporting figures and tables

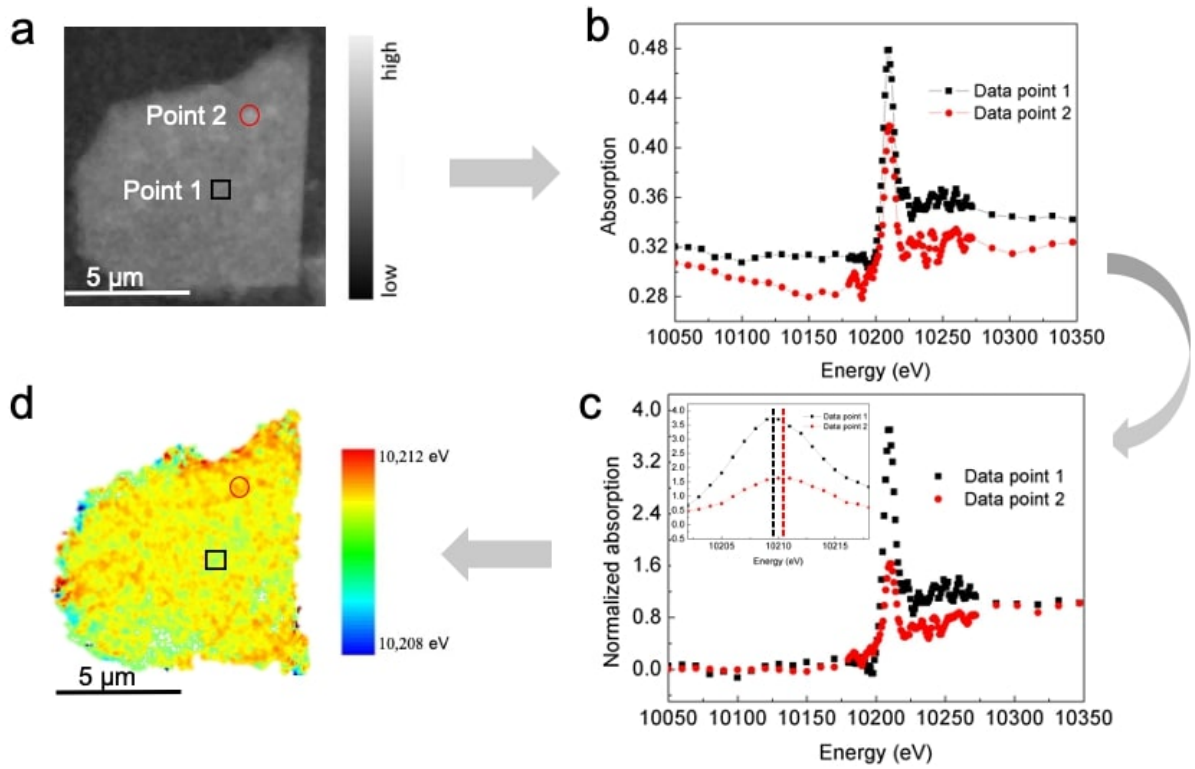

Fig. S1 Explanation of the TXM data normalization protocol. (a) An absorption image of a scratched WO_3 film sample (the one after 600 CV cycles in Fig. 3d) at a specific energy, where the X-ray absorption intensity is indicated by the gradient bar on the right. Two domains with different states of charge were selected to explain the normalization protocol. (b) XANES spectra of the two selected domains before the normalization process. The two spectra marked in (a) exhibit a difference in terms of rising edge energy intensity, suggesting a difference in the absolute amount of W within these two domains (due to the locally different concentrations of W in WO_3

film or different sample thickness). (c) XANES spectra of the two selected domains after the normalization procedure, the pre-edge intensity of the spectra is set to be zero and the post-edge intensity is set to be one. This protocol is applied to normalize all XANES spectra of all pixels of all of the samples presented in this work. The white-line (peak) energy is used to highlight the change of local valence state of W. Two dash lines of the inserted figure indicate the peak energy position of two data points (the black line is for data point 1 and the red line is for data point 2). Data point 2 is shifted to the right relative to data point 1, which means that the local valence state of data point 2 is higher than data point 1. (d) 2D mapping of the local W valence state after the normalization process. Compared with data point 1, data point 2 has a higher valence state and its color is closer to red.

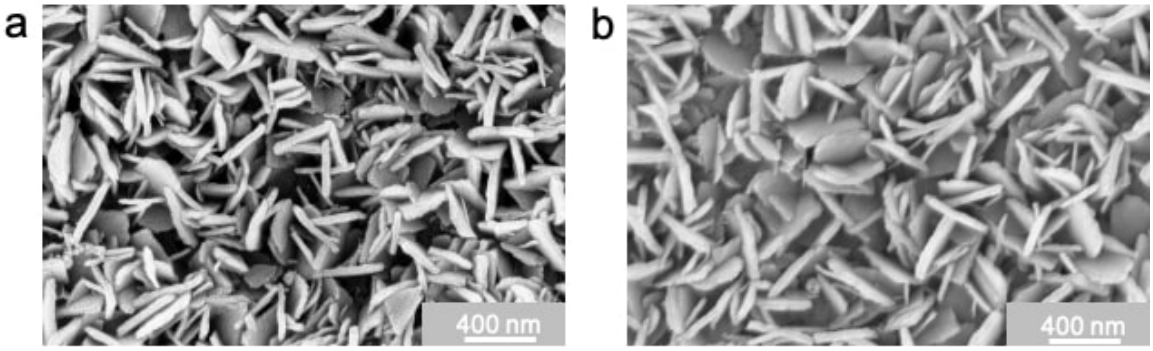

Fig. S2 These newly formed nanoflakes stably exist on the FTO substrate. a) the typical nanoflake formation after 3,000 CV cycles at 60 mV/s with -0.2V-0.6V vs. SCE. b) the nanoflakes after using a 6x20 mm magnetic stirrer to stir the same nanoflake film for 20 hours at 100 rpm. The WO_3 film has a thickness of ~1,000 nm. After long-term stirring, these nanoflakes do not disappear significantly, and the marginal disturbance of the electrolyte caused by stirring is even more severe than that in the flow cell. Therefore, the possibility of these newly formed nanoflakes flowing into the electrolyte is quite low, the main reason for the less formation of nanoflakes is the suppressed redeposition process with a lower concentration of dissolved W species by flowing the electrolyte.

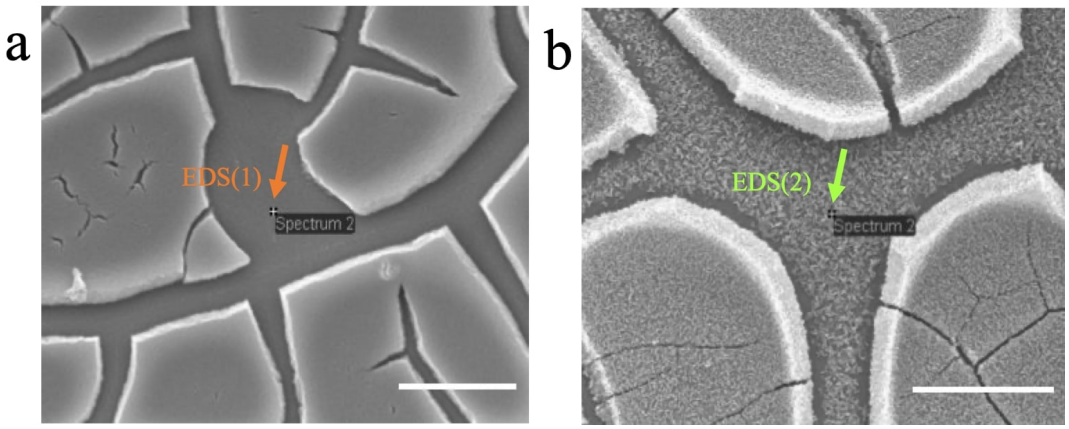

Fig. S3 SEM/EDS of the cracked area of WO_3 film (thickness about 1,000nm) before and after 3,000 CV cycles. (a) The SEM image and the selected cracked area for EDS before electrochemical cycling. (b) The SEM image and the selected cracked area for EDS after 3,000 CV cycles. Scale bars:10 μm.

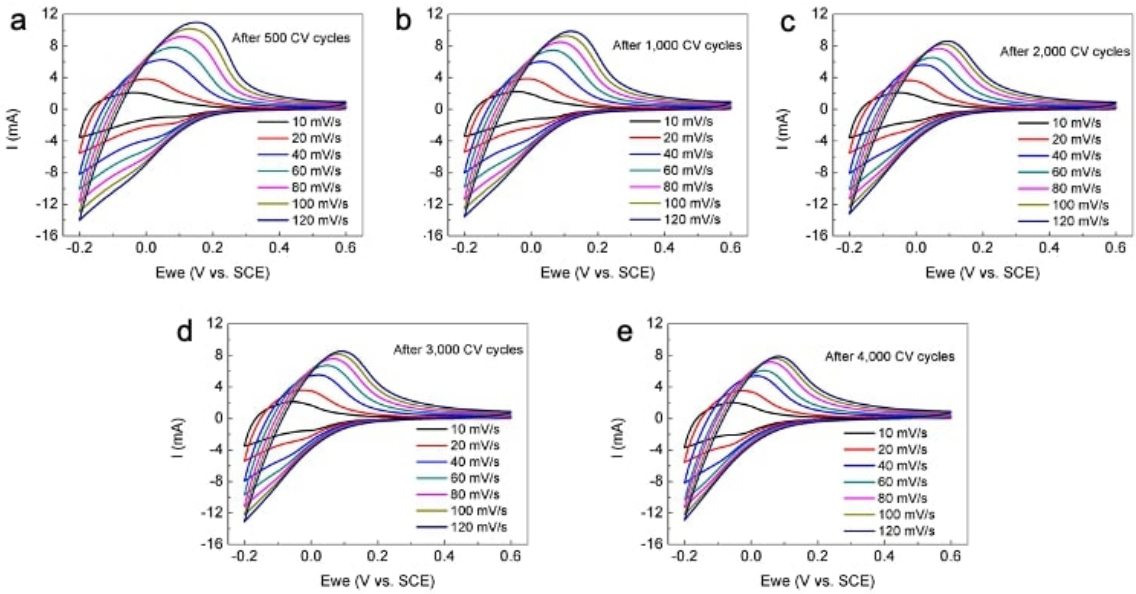

Fig. S4 The CV curves with various scan rates after different number of electrochemical cycling. The various scan rates including 10, 20, 40, 60, 80, 100, and 120 mV/s are used between long-term CV cycling to calculate the apparent diffusion coefficients. The long-term CV cycling is performed in 0.5M H_2SO_4(aq.) at 60 mV/s with -0.2V-0.6V vs. SCE. (a) after 500 CV cycles, (b) after 1,000 CV cycles, (c) after 2,000 CV cycles, (d) after 3,000 CV cycles, and (e) after 4, 000 CV cycles.

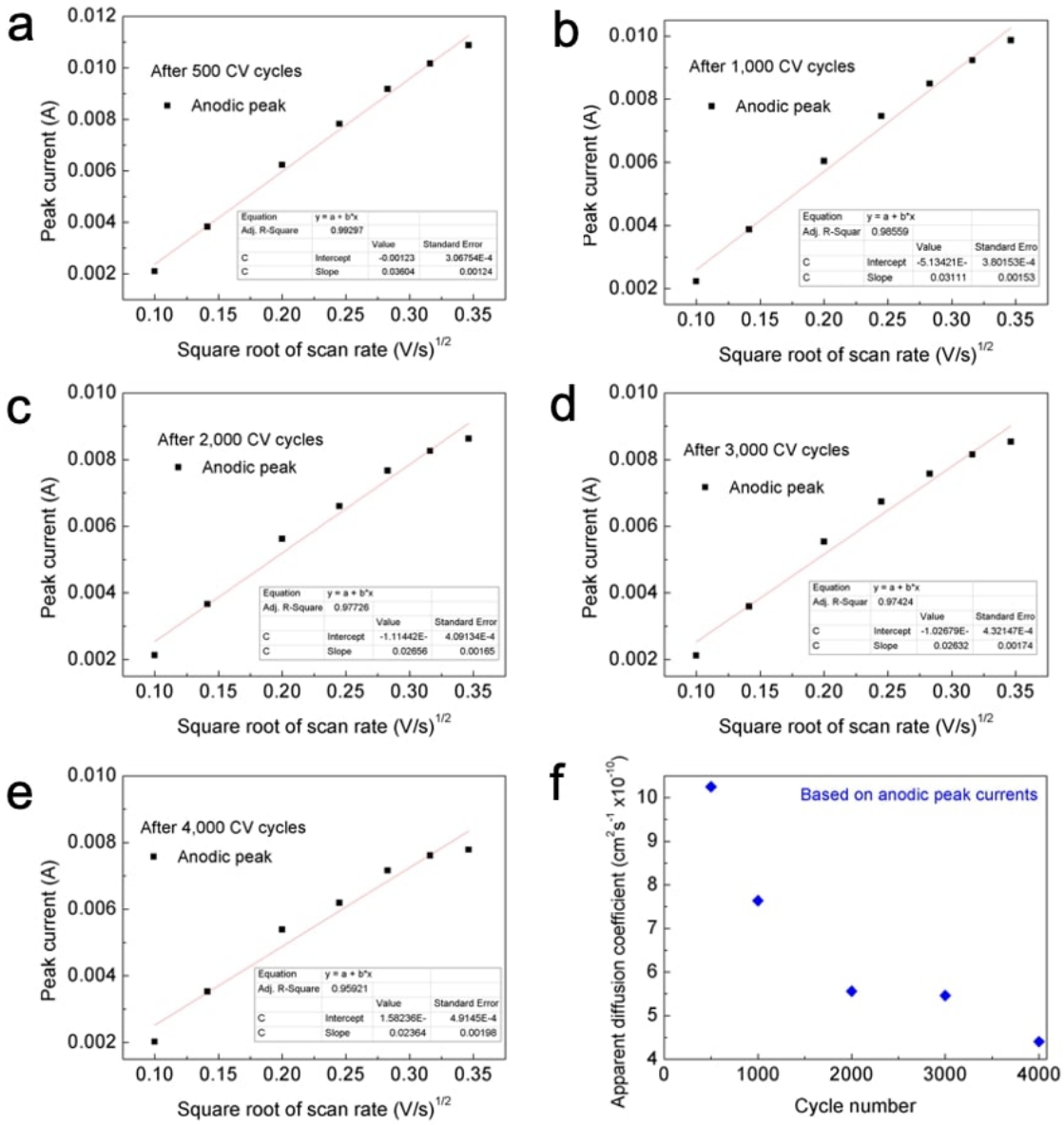

Fig. S5 The evolution of apparent diffusion coefficients during the long-term electrochemical cycling. The calculation of apparent coefficients is based on the Randles–Sevcik equation using various scan rates in CV measurements at room temperature. (a) after 500 CV cycles, (b) after 1,000 CV cycles, (c) after 2,000 CV cycles, (d) after 3,000 CV cycles, and (e) after 4, 000 CV

cycles. The various scan rates including 10, 20, 40, 60, 80, 100, and 120 mV/s are used between long-term CV cycling to calculate the apparent diffusion coefficients. The long-term CV cycling is performed in 0.5M H_2SO_4(aq.) at 60 mV/s with -0.2V-0.6V vs. SCE. The linear relationship indicates that the proton intercalation/deintercalation process is diffusion-controlled. The film thickness is ~ 1,000 nm. (f), Calculated apparent diffusion coefficients decrease with the increase of CV cycle numbers based on anodic peak currents.

Randles–Sevcik equation at room temperature (25 °C):

$$i_p = 0.4463nFAC\left(\frac{nF\upsilon D}{RT}\right)^{0.5}$$

i_p = current maximum in amps

n = number of electrons transferred in the redox event (usually 1)

A = electrode area in cm^2, 4.1875 cm^2

F = Faraday Constant in C mol^{-1}, 96485.3 C mol^{-1}

D = diffusion coefficient in cm^2 s^{-1}

C = concentration in mol/cm^3, 0.001 mol cm^{-3}

ν = scan rate in V s^{-1}

R = Gas constant in J K^{-1} mol^{-1}, 8.3145 J K^{-1} mol^{-1}

T = temperature in K, 298.1 5K

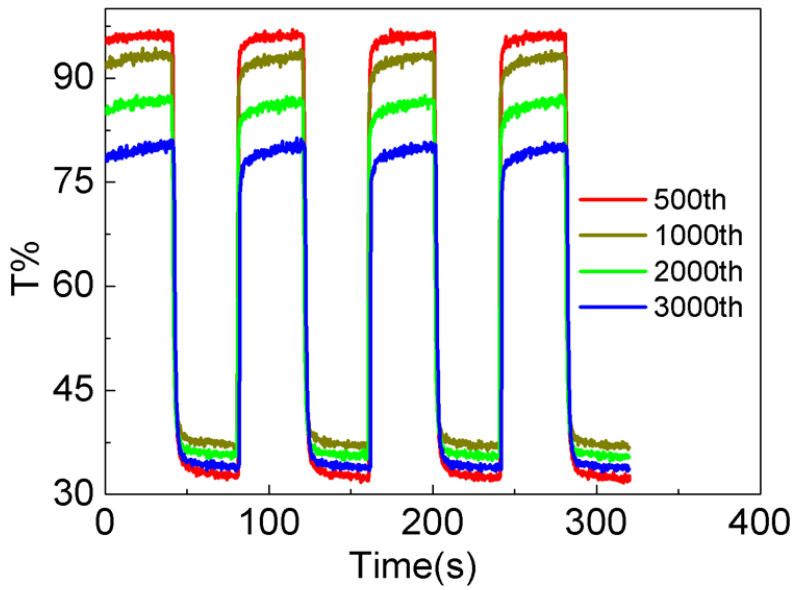

Fig. S6 In-situ transmittance at 600 nm monitoring the evolution of optical modulation during the long-term CV cycling. Chronoamperometry (CA) is performed after the different numbers of CV cycles in the regular cell. The test conditions of CA between the long-term CV cycling are holding 40s at 0.6V vs. SCE.(bleaching) and subsequently holding 40s at -0.2V vs. SCE. (coloration), repeated four times. The optical modulation measured by CA is greater than that measured by CV because the films are maintained for a longer time under both positive and negative potentials.

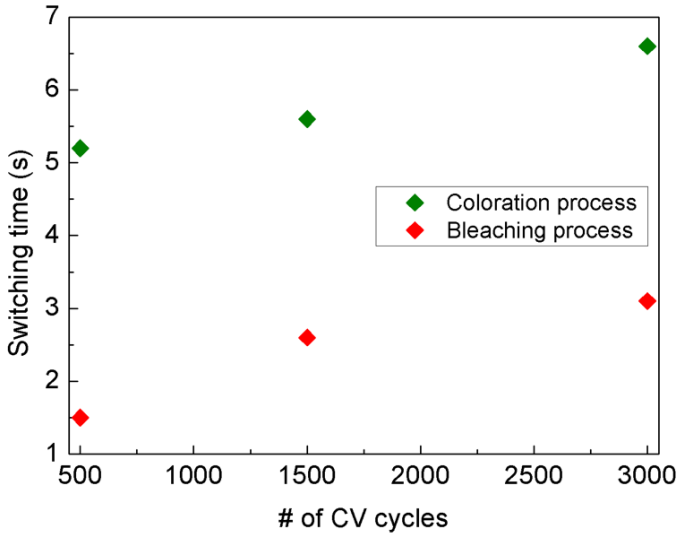

Fig. S7 The evolution of switching time during the long-term CV cycling. Chronoamperometry (CA) is performed after the different numbers of CV cycles in the regular cell. The switching time is calculated as the time needed to achieve 90% of transmittance change.

Table S1 The element atomic ratio of two EDS measurements in Figure S3. The orange color indicates the EDS (1), which is the cracked area before the long-term CV cycling; The green color indicates the EDS (2), which is the cracked area after 3,000 CV cycles. The W atomic ratio is clearly increased after the long-term CV cycling. Sn and Si elements are from the FTO substrate.

Element	at. %	at. %
O	69.7	74.8
Si	14.4	8.8
Sn	15.5	14.0
W	0.4	2.4

Table S2 Based on the XPS data in Figure 3b, the atomic ratios of W^{5+} and W^{6+} are calculated in the WO_3 film before and after 3,000 CV cycles.

Oxidation state of W	Pristine film	Cycled film
+6	90.3%	80.1%
+5	9.7%	19.9%

Table S3 The linear fitting of the square root of scan rates and the anodic peak currents based on Figure S5. Based on the anodic peak current data, the calculated apparent diffusion coefficients decreases along with the increasing number of CV cycles. The cathodic peak is ill-defined so the cathodic peak current is not selected to indicate the trend.

Total # of cycles	Slope (Oxi.)	**D_{anodic} (cm^2s^{-1})**
500	0.036	$1.02*10^{-9}$
1000	0.031	$7.63*10^{-10}$
2000	0.027	$5.56*10^{-10}$
3000	0.026	$5.46*10^{-10}$
4000	0.024	$4.40*10^{-10}$

2.7. Acknowledgment

The work is supported by the Virginia Tech Department of Chemistry startup funds and the Institute for Critical Technology and Applied Science. Use of the Stanford Synchrotron Radiation Lightsource, SLAC National Accelerator Laboratory, is supported by the US Department of Energy, Office of Science, Office of Basic Energy Sciences under Contract No.DE-AC02-76SF00515. The engineering support from D. Van Campen, D. Day, and V. Borzenets for the TXM experiment at beamline 6-2c of SSRL is gratefully acknowledged. This work was performed in part at the Surface Analysis Laboratory in the Department of Chemistry at Virginia Tech, which is supported by the National Science Foundation under Grant No. CHE-1531834. The authors thank Dr. Xu Feng for the technical assistance of XPS measurements.

2.8. References

1. Wen, R. T.; Granqvist, C. G.; Niklasson, G. A., Eliminating degradation and uncovering ion-trapping dynamics in electrochromic WO3 thin films. *Nat Mater* **2015,** *14* (10), 996-1001.

2. Manthiram, A., A reflection on lithium-ion battery cathode chemistry. *Nature Communications* **2020,** *11* (1).

3. Llordes, A.; Garcia, G.; Gazquez, J.; Milliron, D. J., Tunable near-infrared and visible-light transmittance in nanocrystal-in-glass composites. *Nature* **2013,** *500* (7462), 323-326.

4. Llordés, A.; Wang, Y.; Fernandez-Martinez, A.; Xiao, P.; Lee, T.; Poulain, A.; Zandi, O.; Saez Cabezas, C. A.; Henkelman, G.; Milliron, D. J., Linear topology in amorphous metal oxide electrochromic networks obtained via low-temperature solution processing. *Nat Mater* **2016,** *15* (12), 1267-1273.

5. Wang, Z.; Wang, X.; Cong, S.; Chen, J.; Sun, H.; Chen, Z.; Song, G.; Geng, F.; Chen, Q.; Zhao, Z., Towards full-colour tunability of inorganic electrochromic devices using ultracompact fabry-perot nanocavities. *Nature Communications* **2020,** *11* (1), 302.

6. Davy, N. C.; Sezen-Edmonds, M.; Gao, J.; Lin, X.; Liu, A.; Yao, N.; Kahn, A.; Loo, Y. L., Pairing of near-ultraviolet solar cells with electrochromic windows for smart management of the solar spectrum. *Nat Energy* **2017,** *2* (8).

7. Islam, S. M.; Hernandez, T. S.; McGehee, M. D.; Barile, C., Hybrid dynamic windows using reversible metal electrodeposition and ion insertion. *Nat Energy* **2019,** *4* (3), 223-229.

8. Wen, R. T.; Niklasson, G. A.; Granqvist, C. G., Strongly Improved Electrochemical Cycling Durability by Adding Iridium to Electrochromic Nickel Oxide Films. *Acs Appl Mater Inter* **2015,** *7* (18), 9319-9322.

9. Hopmann, E.; Elezzabi, A. Y., Electrochemical Stability Enhancement of Electrochromic Tungsten Oxide by Self-Assembly of a Phosphonate Protection Layer. *Acs Appl Mater Inter* **2020,** *12* (1), 1930-1936.

10. Granqvist, C. G.; Arvizu, M. A.; Qu, H. Y.; Wen, R. T.; Niklasson, G. A., Advances in electrochromic device technology: Multiple roads towards superior durability. *Surf Coat Tech* **2019,** *357*, 619-625.

11. Zhang, S. L.; Cao, S.; Zhang, T. R.; Fisher, A.; Lee, J. Y., Al3+ intercalation/de-intercalation-enabled dual-band electrochromic smart windows with a high optical modulation, quick response and long cycle life. *Energ Environ Sci* **2018,** *11* (10), 2884-2892.

12. Lee, S. H.; Deshpande, R.; Parilla, P. A.; Jones, K. M.; To, B.; Mahan, A. H.; Dillon, A. C., Crystalline WO3 nanoparticles for highly improved electrochromic applications. *Adv Mater* **2006,** *18* (6), 763-766.

13. Niklasson, G. A.; Granqvist, C. G., Electrochromics for smart windows: thin films of tungsten oxide and nickel oxide, and devices based on these. *J Mater Chem* **2007,** *17* (2), 127-156.

14. Granqvist, C. G., Electrochromics for smart windows: Oxide-based thin films and devices. *Thin Solid Films* **2014,** *564*, 1-38.

15. Dickens, P. G.; Hurditch, R. J., X-Ray and Neutron Diffraction Studies of a Tetragonal Hydrogen Bronze Hxwo3. *Nature* **1967,** *215* (5107), 1266-1267.

16. Deb, S. K., Opportunities and challenges in science and technology of WO3 for electrochromic and related applications. *Sol Energ Mat Sol C* **2008,** *92* (2), 245-258.

17. Neto, J. D. M.; Torresi, R. M.; de Torresi, S. I. C., Electrochromic behavior of WO3 nanoplate thin films in acid aqueous solution and a protic ionic liquid. *J Electroanal Chem* **2016,** *765*, 111-117.

18. Wen, R. T.; Malmgren, S.; Granqvist, C. G.; Niklasson, G. A., Degradation Dynamics for Electrochromic WO3 Films under Extended Charge Insertion and Extraction: Unveiling Physicochemical Mechanisms. *Acs Appl Mater Inter* **2017,** *9* (14), 12872-12877.

19. Dong, D. M.; Wang, W. W.; Rougier, A.; Barnabe, A.; Dong, G. B.; Zhang, F.; Diao, X. G., Lithium trapping as a degradation mechanism of the electrochromic properties of all-solid-state WO3//NiO devices. *J Mater Chem C* **2018,** *6* (37), 9875-9889.

20. Wen, R. T.; Arvizu, M. A.; Morales-Luna, M.; Granqvist, C. G.; Niklasson, G. A., Ion Trapping and Detrapping in Amorphous Tungsten Oxide Thin Films Observed by Real-Time Electro-Optical Monitoring. *Chem Mater* **2016,** *28* (13), 4670-4676.

21. An, S. J.; Li, J. L.; Daniel, C.; Mohanty, D.; Nagpure, S.; Wood, D. L., The state of understanding of the lithium-ion-battery graphite solid electrolyte interphase (SEI) and its relationship to formation cycling. *Carbon* **2016,** *105*, 52-76.

22. He, Y.; Gu, M.; Xiao, H. Y.; Luo, L. L.; Shao, Y. Y.; Gao, F.; Du, Y. G.; Mao, S. X.; Wang, C. M., Atomistic Conversion Reaction Mechanism of WO3 in Secondary Ion Batteries of Li, Na, and Ca. *Angew Chem Int Edit* **2016,** *55* (21), 6244-6247.

23. Jung, H.; Taillefert, M.; Sun, J.; Wang, Q.; Borkiewicz, O. J.; Liu, P.; Yang, L.; Chen, S.; Chen, H.; Tang, Y., Redox Cycling Driven Transformation of Layered Manganese Oxides to Tunnel Structures. *Journal of the American Chemical Society* **2020,** *142* (5), 2506-2513.

24. Zheng, H. D.; Ou, J. Z.; Strano, M. S.; Kaner, R. B.; Mitchell, A.; Kalantar-Zadeh, K., Nanostructured Tungsten Oxide - Properties, Synthesis, and Applications. *Adv Funct Mater* **2011,** *21* (12), 2175-2196.

25. Mitchell, J. B.; Geise, N. R.; Paterson, A. R.; Osti, N. C.; Sun, Y. Y. L.; Fleischmann, S.; Zhang, R.; Madsen, L. A.; Toney, M. F.; Jiang, D. E.; Kolesnikov, A. I.; Mamontov, E.; Augustyn, V., Confined Interlayer Water Promotes Structural Stability for High-Rate Electrochemical Proton Intercalation in Tungsten Oxide Hydrates. *Acs Energy Lett* **2019,** *4* (12), 2805-2812.

26. Yang, Y.; Xu, R.; Zhang, K.; Lee, S. J.; Mu, L. Q.; Liu, P. F.; Waters, C. K.; Spence, S.; Xu, Z. R.; Wei, C. X.; Kautz, D. J.; Yuan, Q. X.; Dong, Y. H.; Yu, Y. S.; Xiao, X. H.; Lee, H. K.; Pianetta, P.; Cloetens, P.; Lee, J. S.; Zhao, K. J.; Lin, F.; Liu, Y. J., Quantification of Heterogeneous Degradation in Li-Ion Batteries. *Adv Energy Mater* **2019,** *9* (25).

27. Tian, C. X.; Xu, Y. H.; Nordlund, D.; Lin, F.; Liu, J.; Sun, Z. H.; Liu, Y. J.; Doeff, M., Charge Heterogeneity and Surface Chemistry in Polycrystalline Cathode Materials. *Joule* **2018,** *2* (3), 464-477.

28. Mu, L. Q.; Yuan, Q. X.; Tian, C. X.; Wei, C. X.; Zhang, K.; Liu, J.; Pianetta, P.; Doeff, M. M.; Liu, Y. J.; Lin, F., Propagation topography of redox phase transformations in heterogeneous layered oxide cathode materials. *Nature Communications* **2018,** *9*.

29. Xu, Z.; Jiang, Z.; Kuai, C.; Xu, R.; Qin, C.; Zhang, Y.; Rahman, M. M.; Wei, C.; Nordlund, D.; Sun, C.-J.; Xiao, X.; Du, X.-W.; Zhao, K.; Yan, P.; Liu, Y.; Lin, F., Charge distribution guided by grain crystallographic orientations in polycrystalline battery materials. *Nature Communications* **2020,** *11* (1), 83.

30. Lin, F.; Cheng, J. F.; Engtrakul, C.; Dillon, A. C.; Nordlund, D.; Moore, R. G.; Weng, T. C.; Williams, S. K. R.; Richards, R. M., In situ crystallization of high performing WO3-based electrochromic materials and the importance for durability and switching kinetics. *J Mater Chem* **2012,** *22* (33), 16817-16823.

31. Liu, Y. J.; Meirer, F.; Williams, P. A.; Wang, J. Y.; Andrews, J. C.; Pianetta, P., TXM-Wizard: a program for advanced data collection and evaluation in full-field transmission X-ray microscopy. *J Synchrotron Radiat* **2012,** *19*, 281-287.

32. Li, C. P.; Lin, F.; Richards, R. M.; Engtrakul, C.; Dillon, A. C.; Tenent, R. C.; Wolden, C. A., Ultrasonic spray deposition of high performance WO3 films using template-assisted sol-gel chemistry. *Electrochem Commun* **2012,** *25*, 62-65.

33. Li, C. P.; Lin, F.; Richards, R. M.; Engtrakul, C.; Tenent, R. C.; Wolden, C. A., The influence of sol-gel processing on the electrochromic properties of mesoporous WO3 films produced by ultrasonic spray deposition. *Sol Energ Mat Sol C* **2014,** *121*, 163-170.

34. Gavrilko, T. A.; Stepkin, V. I.; Shiyanovskaya, I. V., Ir and Optical Spectroscopy of Structural-Changes of Wo3 Electrochromic Thin-Films. *J Mol Struct* **1990,** *218*, 411-416.

35. Lin, F.; Li, C. P.; Chen, G.; Tenent, R. C.; Wolden, C. A.; Gillaspie, D. T.; Dillon, A. C.; Richards, R. M.; Engtrakul, C., Low-temperature ozone exposure technique to modulate the stoichiometry of WOx nanorods and optimize the electrochromic performance. *Nanotechnology* **2012,** *23* (25).

36. Kim, H.; Choi, D.; Kim, K.; Chu, W.; Chun, D. M.; Lee, C. S., Effect of particle size and amorphous phase on the electrochromic properties of kinetically deposited WO3 films. *Sol Energ Mat Sol C* **2018,** *177*, 44-50.

37. Xia, Y.; Xiong, Y.; Lim, B.; Skrabalak, S. E., Shape-Controlled Synthesis of Metal Nanocrystals: Simple Chemistry Meets Complex Physics? *Angew Chem Int Edit* **2009,** *48* (1), 60-103.

38. Pacholski, C.; Kornowski, A.; Weller, H., Self-Assembly of ZnO: From Nanodots to Nanorods. *Angew Chem Int Edit* **2002,** *41* (7), 1188-1191.

39. Arnoldussen, T. C., A Model for Electrochromic Tungstic Oxide Microstructure and Degradation. *J Electrochem Soc* **1981,** *128* (1), 117-123.

40. Nave, M. I.; Kornev, K. G., Complexity of Products of Tungsten Corrosion: Comparison of the 3D Pourbaix Diagrams with the Experimental Data. *Metall Mater Trans A* **2017,** *48a* (3), 1414-1424.

41. Lee, Y. J.; Lee, T.; Soon, A., Phase Stability Diagrams of Group 6 Magneli Oxides and Their Implications for Photon-Assisted Applications. *Chem Mater* **2019,** *31* (11), 4282-4290.

42. Fuladpanjeh-Hojaghan, B.; Elsutohy, M. M.; Kabanov, V.; Heyne, B.; Trifkovic, M.; Roberts, E. P. L., In-Operando Mapping of pH Distribution in Electrochemical Processes. *Angew Chem Int Edit* **2019,** *58* (47), 16815-16819.

43. Li, W. J.; Da, P. M.; Zhang, Y. Y.; Wang, Y. C.; Lin, X.; Gong, X. G.; Zheng, G. F., WO3 Nanoflakes for Enhanced Photoelectrochemical Conversion. *Acs Nano* **2014,** *8* (11), 11770-11777.

44. Kong, W.; Zhang, X.; Liu, S.; Zhou, Y.; Chang, B.; Zhang, S.; Fan, H.; Yang, B., N Doped Carbon Dot Modified WO3 Nanoflakes for Efficient Photoelectrochemical Water Oxidation. *Adv Mater Interfaces* **2019,** *6* (1), 1801653.

45. Kamal, H.; Akl, A. A.; Abdel-Hady, K., Influence of proton insertion on the conductivity, structural and optical properties of amorphous and crystalline electrochromic WO3 films. *Physica B* **2004,** *349* (1-4), 192-205.

46. Lin, F.; Nordlund, D.; Markus, I. M.; Weng, T. C.; Xin, H. L.; Doeff, M. M., Profiling the nanoscale gradient in stoichiometric layered cathode particles for lithium-ion batteries. *Energ Environ Sci* **2014,** *7* (9), 3077-3085.

47. Purans, J.; Kuzmin, A.; Parent, P.; Laffon, C., X-ray absorption study of the electronic structure of tungsten and molybdenum oxides on the OK-edge. *Electrochim Acta* **2001,** *46* (13-14), 1973-1976.

48. Suntivich, J.; Hong, W. T.; Lee, Y. L.; Rondinelli, J. M.; Yang, W. L.; Goodenough, J. B.; Dabrowski, B.; Freeland, J. W.; Shao-Horn, Y., Estimating Hybridization of Transition Metal and Oxygen States in Perovskites, from O K-edge X-ray Absorption Spectroscopy. *J Phys Chem C* **2014,** *118* (4), 1856-1863.

49. Sun, S.; Wu, J.; Watanabe, M.; Akbay, T.; Ishihara, T., Single-Electron-Trapped Oxygen Vacancy on Ultrathin WO3·0.33H2O {100} Facets Suppressing Backward Reaction for Promoted H2 Evolution in Pure Water Splitting. *The Journal of Physical Chemistry Letters* **2019,** *10* (11), 2998-3005.

50. Cong, S.; Tian, Y. Y.; Li, Q. W.; Zhao, Z. G.; Geng, F. X., Single-Crystalline Tungsten Oxide Quantum Dots for Fast Pseudocapacitor and Electrochromic Applications. *Adv Mater* **2014,** *26* (25), 4260-4267.

51. Jayarathne, U.; Chandrasekaran, P.; Greene, A. F.; Mague, J. T.; DeBeer, S.; Lancaster, K. M.; Sproules, S.; Donahue, J. P., X-ray Absorption Spectroscopy Systematics at the Tungsten L-Edge. *Inorg Chem* **2014,** *53* (16), 8230-8241.

52. Yamazoe, S.; Hitomi, Y.; Shishido, T.; Tanaka, T., XAFS study of tungsten L-1- and L-3-edges: Structural analysis of WO3 species loaded on TiO2 as a catalyst for photo-oxidation of NH3. *J Phys Chem C* **2008,** *112* (17), 6869-6879.

53. Meirer, F.; Cabana, J.; Liu, Y. J.; Mehta, A.; Andrews, J. C.; Pianetta, P., Three-dimensional imaging of chemical phase transformations at the nanoscale with full-field transmission X-ray microscopy. *J Synchrotron Radiat* **2011,** *18*, 773-781.

54. Gent, W. E.; Li, Y. Y.; Ahn, S.; Lim, J.; Liu, Y. J.; Wise, A. M.; Gopal, C. B.; Mueller, D. N.; Davis, R.; Weker, J. N.; Park, J. H.; Doo, S. K.; Chueh, W. C., Persistent State-of-Charge Heterogeneity in Relaxed, Partially Charged Li1-xNi1/3Co1/3Mn1/3O2 Secondary Particles. *Adv Mater* **2016,** *28* (31), 6631-6638.

55. Evans, R. C.; Ellingworth, A.; Cashen, C. J.; Weinberger, C. R.; Sambur, J. B., Influence of single-nanoparticle electrochromic dynamics on the durability and speed of smart windows. *P Natl Acad Sci USA* **2019,** *116* (26), 12666-12671.

56. Wang, X.; Chen, K.; de Vasconcelos, L. S.; He, J.; Shin, Y. C.; Mei, J.; Zhao, K., Mechanical breathing in organic electrochromics. *Nature Communications* **2020,** *11* (1), 211.

57. Bouessay, I.; Rougier, A.; Tarascon, J. M., Electrochemically inactive nickel oxide as electrochromic material. *J Electrochem Soc* **2004,** *151* (6), H145-H152.

58. Lin, F.; Bult, J. B.; Nanayakkara, S.; Dillon, A. C.; Richards, R. M.; Blackburn, J. L.; Engtrakul, C., Graphene as an Efficient Interfacial Layer for Electrochromic Devices. *Acs Appl Mater Inter* **2015,** *7* (21), 11330-11336.

59. Whittingham, M. S., Hydrogen motion in oxides: from insulators to bronzes. *Solid State Ionics* **2004,** *168* (3-4), 255-263.

60. Lin, H.; Zhou, F.; Liu, C. P.; Ozolins, V., Non-Grotthuss proton diffusion mechanism in tungsten oxide dihydrate from first-principles calculations. *J Mater Chem A* **2014,** *2* (31), 12280-12288.

61. Mukherjee, R.; Sahay, P. P., Improved electrochromic performance in sprayed WO3 thin films upon Sb doping. *J Alloy Compd* **2016,** *660*, 336-341.

62. Heo, S.; Dahlman, C. J.; Staller, C. M.; Jiang, T.; Dolocan, A.; Korgel, B. A.; Milliron, D. J., Enhanced Coloration Efficiency of Electrochromic Tungsten Oxide Nanorods by Site Selective Occupation of Sodium Ions. *Nano Lett* **2020,** *20* (3), 2072-2079.

3. Conclusions

3.1. Investigating the solid–liquid interface and its influence on the bulk electrode.

There are few fundamental systematic studies on the mechanism of degradation of electrochromic active materials during long-term electrochemical cycling. Here, we have found dramatic morphology evolution of the WO_3 material and believe it to be one of the main mechanisms of degradation upon long-term electrochemical cycling in the aqueous acid electrolyte. The mass transport across the electrochemical interface during electrochemical cycling leads to dynamic speciation such as repeated ion dissolution and redeposition, which creates a micro-environment for nanoscale morphological evolution. Therefore, it is insightful to further investigate the mechanism of transition metal oxide dissolution and redeposition behaviors at the highly reactive electrochemical interface and to identify how different states of electrochemical cycling will trigger different speciation variations in the electrochemical interfacial region.[1] Also, the tunable substrate thickness and controllable electrochemical cycling conditions can be manipulated to uncover the underlying relationship between dynamics speciation, concentration gradient, and local pH gradient at the electrochemical interface, especially the diffusion layer.[2-4]

With obtaining this knowledge, the degraded performance could also be restored by reversibly adjusting the interfacial nanostructures, and the induced structural evolution of the bulk electrode could be suppressed, thus improving the overall electrochemical performance.

3.2. Clarifying the uncertain role of electrode nanostructure design.

The electrochemical community has adopted many approaches to lower the charge transfer resistance in the interfacial region such as increasing the surface area of electrodes to facilitate electrolyte infiltration and shortening the ion diffusion length. One of the most representative approaches is to design specific nanostructures of the electrode including but not limited to nanorods, nanoflakes, nanospheres, nanoflowers, etc.[5-7] These certain nanostructures are typically prepared by wet chemical synthesis and electrodeposition methods.[8, 9] However, the enormous morphological changes discovered during the long-term electrochemical cycling, reported in this thesis, may question the practical effectiveness of the pre-designed nanostructures. These specific nanostructures may not exist stably and will gradually evolve due to the local structure reconstruction caused by the dissolution and redeposition of transition metal oxides or the

irreversible ion intercalation during cycling. Therefore, the overall charge transfer process would correspondingly undergo great changes, and the benefit of a delicate nanostructure design used to improve electrochemical cycling may not remain stable and effective, especially in the interfacial region. Therefore, it is important to probe and investigate the morphological evolution or the surface reconstruction at relevant length scales under the electrochemical operating conditions, which can greatly clarify the role of the nanostructure design of electrode materials.

3.3. References

1. Brown, G. E.; Henrich, V. E.; Casey, W. H.; Clark, D. L.; Eggleston, C.; Felmy, A.; Goodman, D. W.; Gratzel, M.; Maciel, G.; McCarthy, M. I.; Nealson, K. H.; Sverjensky, D. A.; Toney, M. F.; Zachara, J. M., Metal oxide surfaces and their interactions with aqueous solutions and microbial organisms. *Chem Rev* **1999,** *99* (1), 77-174.
2. Velasco-Velez, J. J.; Wu, C. H.; Pascal, T. A.; Wan, L. W. F.; Guo, J. H.; Prendergast, D.; Salmeron, M., The structure of interfacial water on gold electrodes studied by x-ray absorption spectroscopy. *Science* **2014,** *346* (6211), 831-834.
3. Fuladpanjeh-Hojaghan, B.; Elsutohy, M. M.; Kabanov, V.; Heyne, B.; Trifkovic, M.; Roberts, E. P. L., In-Operando Mapping of pH Distribution in Electrochemical Processes. *Angew Chem Int Edit* **2019,** *58* (47), 16815-16819.
4. Rakov, D. A.; Chen, F. F.; Ferdousi, S. A.; Li, H.; Pathirana, T.; Simonov, A. N.; Howlett, P. C.; Atkin, R.; Forsyth, M., Engineering high-energy-density sodium battery anodes for improved cycling with superconcentrated ionic-liquid electrolytes. *Nat Mater* **2020**.

5. Ma, D. Y.; Shi, G. Y.; Wang, H. Z.; Zhang, Q. H.; Li, Y. G., Morphology-tailored synthesis of vertically aligned 1D WO3 nano-structure films for highly enhanced electrochromic performance. *J Mater Chem A* **2013,** *1* (3), 684-691.

6. Li, Y. Q.; Chen, D. H.; Caruso, R. A., Enhanced electrochromic performance of WO3 nanowire networks grown directly on fluorine-doped tin oxide substrates. *J Mater Chem C* **2016,** *4* (44), 10500-10508.

7. Heo, S.; Cho, S. H.; Dahlman, C. J.; Agrawal, A.; Milliron, D. J., Influence of Crystalline and Shape Anisotropy on Electrochromic Modulation in Doped Semiconductor Nanocrystals. *Acs Energy Lett* **2020**, 2662-2670.

8. Li, Y.; McMaster, W. A.; Wei, H.; Chen, D.; Caruso, R. A., Enhanced Electrochromic Properties of WO3 Nanotree-like Structures Synthesized via a Two-Step Solvothermal Process Showing Promise for Electrochromic Window Application. *ACS Applied Nano Materials* **2018,** *1* (6), 2552-2558.

9. Pan, J. B.; Wang, Y.; Zheng, R. Z.; Wang, M. T.; Wan, Z. Q.; Jia, C. Y.; Weng, X. L.; Xie, J. L.; Deng, L. J., Directly grown high-performance WO3 films by a novel one-step hydrothermal method with significantly improved stability for electrochromic applications. *J Mater Chem A* **2019,** *7* (23), 13956-13967.